Atmos. Chem. Phys., 24, 14145–14175, 2024
https://doi.org/10.5194/acp-24-14145-2024

Atmospheric Chemistry and Physics
Open Access
EGU

The impact of the mesh size and microphysics scheme on the representation of mid-level clouds in the ICON model in hilly and complex terrain

Nadja Omanovic[1,★], **Brigitta Goger**[2,★], **and Ulrike Lohmann**[1]

[1]Institute for Atmospheric and Climate Science, ETH Zürich, Zurich, Switzerland
[2]Center for Climate Systems Modeling (C2SM), ETH Zürich, Zurich, Switzerland
★These authors contributed equally to this work.

Correspondence: Nadja Omanovic (nadja.omanovic@env.ethz.ch) and Brigitta Goger (brigitta.goger@c2sm.ethz.ch)

Received: 28 June 2024 – Discussion started: 29 July 2024
Revised: 31 October 2024 – Accepted: 5 November 2024 – Published: 19 December 2024

Abstract. The rise in computational power in recent years has enabled research and national weather services to conduct high-resolution simulations down to the kilometric ($\Delta x = \mathcal{O}(1\,\mathrm{km})$) and even to hectometric ($\Delta x = \mathcal{O}(100\,\mathrm{m})$) scales for both weather and climate applications. We investigate with the state-of-the-art numerical weather prediction model ICON how mid-level clouds are represented on a mesh size of 1 km and 65 m, respectively, and for two bulk microphysics schemes, namely one-moment and two-moment cloud microphysics. For this analysis, we leverage the abundant observational data from two independent field campaigns in Switzerland (CLOUDLAB; hilly terrain) and Austria (CROSSINN; complex terrain). With four case studies, we show that while the temperature fields around the campaign sites are well represented in both mesh sizes, the 65 m resolution simulates a more realistic vertical velocity structure that is beneficial for cloud formation. Therefore, the largest differences for the representation of clouds lie in the two mesh sizes. The 1 km simulation in hilly terrain does not capture the observed clouds in both cloud microphysics schemes. Here, the higher resolution of the vertical velocities in the 65 m proves to be crucial for representing the investigated cloud types, and the two-moment microphysics scheme in general performs better with respect to the cloud characteristics because it considers variations in cloud droplet and ice crystal number concentrations. In complex terrain, the differences between the mesh sizes and the cloud microphysics schemes are surprisingly small, but the 65 m simulations with two-moment cloud microphysics show the most realistic cloud representation.

1 Introduction

Numerical weather prediction (NWP) models have undergone immense improvements in the last few decades due to the increase in the computational power (Bauer et al., 2015; Palmer, 2017). Nowadays, operational NWP forecasts run at the kilometric range at various European weather services (e.g., MeteoSwiss with ICON at $\Delta x = 1\,\mathrm{km}$ (https://www.meteoswiss.admin.ch/about-us/research-and-cooperation/projects/2023/icon-22.html, last access: 16 December 2024), UK Met Office with UM at $\Delta x = 1.5\,\mathrm{km}$ (https://www.metoffice.gov.uk/research/approach/modelling-systems/unified-model/weather-forecasting, last access: 16 December 2024), and Météo France with AROME at $\Delta x = 1.25\,\mathrm{km}$ (https://donneespubliques.meteofrance.fr/?fond=produit&id_produit=131&id_rubrique=51, last access: 16 December 2024)), and kilometer-scale climate models with their high-resolution output fields (e.g., precipitation) have become more and more common for regional (e.g., Ban et al., 2014; Leutwyler et al., 2016), as well as global, simulations (Schär et al., 2020; Hohenegger et al., 2023).

One of the major advantages of kilometric simulations ($\Delta x = \mathcal{O}(1\,\mathrm{km})$) is the more realistic representation of model topography in the domains, allowing for more detailed terrain-induced circulations in models, such as the thermally induced valley wind system (Schmidli et al., 2018; Goger et al., 2018, 2019; Heim et al., 2020; Mikkola et al., 2023). Another advantage of kilometric simulations compared to coarser-mesh sizes ($\Delta x = \mathcal{O}(10\,\mathrm{km})$) is that the mass flux parameterization can be switched off because deep convection is already resolved on the grid (Chow et al., 2019). Hentgen et al. (2019) point out the improved representation of clouds in kilometric simulations over Europe, and more recent studies even suggest going towards the hectometric range ($\Delta x = \mathcal{O}(100\,\mathrm{m})$), further improving cloud representation in numerical models (Stevens et al., 2020; Miyamoto et al., 2013). In their simulations at $\Delta x = 100\,\mathrm{m}$ over Germany, Heinze et al. (2017a) noted a more detailed representation of cloud patterns over Germany, and Schemann et al. (2020) compared large-eddy simulations (LESs) to local observations to find the best representation of clouds in the model in small domains with realistic mesoscale forcing. Therefore, LESs are favorable for process studies, also because local circulations and the boundary layer structure affecting cloud formation are represented well if realistic atmospheric forcing (e.g., from kilometric NWP model runs) and high-quality surface parameter datasets are used (e.g., Heinze et al., 2017b; Gerber et al., 2018; Umek et al., 2021; Goger et al., 2022; Rohanizadegan et al., 2023; Goger and Dipankar, 2024; Voordendag et al., 2024). Still, there are limitations to the ability to interpret LES results, given that many cloud processes act on a submicron scale and thus still need to be parameterized. Nevertheless, LESs proved to be a useful tool for investigating, e.g., marine boundary layer clouds given their inadequate representation in global models (e.g., Stevens and Bretherton, 1999; Nam et al., 2012). This includes studies ranging from investigating the effect of dynamics, such as entrainment (e.g., Siebesma et al., 2003; Duynkerke et al., 2004; Bretherton et al., 2007; Sandu and Stevens, 2011; Bretherton and Blossey, 2017; Jeong et al., 2023) to aerosol–cloud interactions (e.g., Jiang et al., 2002; Xue et al., 2008; Sandu et al., 2008; Andrejczuk et al., 2010; Twohy et al., 2013; Tonttila et al., 2017; Atlas et al., 2020; Diamond et al., 2022; Delbeke et al., 2023; Li et al., 2024; Perez et al., 2024). Often, these studies included comparisons to observational data gathered during campaigns targeting marine boundary layer clouds (e.g., Roberts et al., 2010; Allen et al., 2011; Schulze et al., 2020; Wang et al., 2022; Howes et al., 2023), which also led to model improvements with respect to the formulation of parameterizations and numerics (e.g., Stevens et al., 1996; Stevens and Bretherton, 1999; Yamaguchi and Feingold, 2012; Pressel et al., 2017; Mellado et al., 2018). LES studies on clouds over land include the already mentioned model evaluation of ICON in large-eddy mode over Germany (Heinze et al., 2017a; Schemann et al., 2020), the evaluation of shallow cumulus clouds over the Great Plains (Zhang et al., 2017), the more idealized approach of evaluating the impact of turbulence on moist convection (Strauss et al., 2019), the dependence of convection and precipitation on grid spacing (Moseley et al., 2020; Singh et al., 2021), or the formation of clouds over mountainous terrain (Panosetti et al., 2016). All of these studies highlight the advantages of LESs for studying cloud processes.

When focusing on clouds in models, the question arises regarding which level of complexity is needed to "properly" represent them in terms of the parameterizations of clouds. The answer to this question is certainly constrained by the available cloud microphysics schemes in the model but also by the available computing resources. The more complex schemes, which are supposed to be more accurate, also require more computing resources for resolving more processes for cloud formation and evolution. The simplest cloud microphysics schemes are so-called bulk cloud microphysics schemes which specify a selected number of hydrometeor classes (e.g., cloud droplets, ice crystals, snow, rain, graupel, and hail) and directly predict the mass mixing ratios (one-moment cloud microphysics, 1M) or, in addition, the number mixing ratios (two-moment cloud microphysics, 2M) of these hydrometeors. This, however, requires the parameterization of the shape and size distributions of the prognostic particles (Doms et al., 2021). The prediction of both mass and number mixing ratios already results in a large increase in the required computing resources, such that national weather services often perform their operational forecasts with a one-moment cloud microphysics scheme (Buzzi, 2008; Doms et al., 2021). More advanced cloud microphysics schemes include spectral bin microphysics (e.g., Simmel et al., 2002; Khain et al., 2011) or so-called Lagrangian superparticles (e.g., Andrejczuk et al., 2008, 2010; Shima et al., 2009; Hoffmann, 2016). The wide range of possible cloud microphysics schemes also inspired several studies comparing bulk and bin cloud microphysics schemes (e.g., Endo et al., 2015; Zhang et al., 2017; Witte et al., 2022; Sato et al., 2015), Eulerian and Lagrangian frameworks (e.g., Grabowski, 2020), or 1M versus 2M. For the latter, studies pointed out the better performance of 2M, highlighting the potential for better representing clouds in model simulations (e.g., Baldauf et al., 2011; Bryan and Morrison, 2012; Van Weverberg et al., 2014; Kovačević and Ćurić, 2015; Kondo et al., 2021).

In this study, we want to answer the question of whether the two-moment microphysics scheme (2M) is better suited for representing and also studying clouds compared to the one-moment microphysics scheme (1M). We further expand this question by also looking at the dependence of the horizontal resolution ($\Delta x = 1\,\mathrm{km}$ and $\Delta x = 65\,\mathrm{m}$) and the underlying topography (hilly and complex terrain). The evaluation is based on case studies and model–observation comparisons utilizing high-resolution remote sensing observational data from two field campaigns in Switzerland and Austria, respectively. We focus on mid-level clouds with either a

Table 1. Overview of field campaigns, including their respective coordinates, altitude, duration, instruments used in this study, and the selected case studies.

Field campaigns	CLOUDLAB	CROSSINN
Coordinates	47°04′14″ N, 7°52′22″ E	47°18′19″ N, 11°37′19″ E
Altitude	920 m a.m.s.l.	545 m a.m.s.l.
Duration	Jan–Mar 2022 Dec 2022–Feb 2023 Dec 2023–Feb 2024	Jul–Oct 2019
Instruments	All-sky camera Ceilometer CloudNET (–) Microwave radiometer (–)	All-sky camera Ceilometer (–) Lidar Microwave radiometer Radiosondes
Case dates	20 March 2022 31 January 2023	5 August 2019 14 August 2019

stratiform or a more convective character. This work should help us to understand the differences between two bulk microphysics schemes, their benefits, and disadvantages and to highlight limitations in process representation on various grid scales and above different terrains. We first provide an overview of the field sites, campaigns, and the model setup (Sect. 2) before discussing the model performance for hilly terrain (Sect. 3.1) and complex terrain (Sect. 3.2). After a comparison of the case studies and the discussion (Sect. 3.3), we highlight our main findings in the conclusions (Sect. 4).

2 Field campaigns and model setup

In the following, we describe the field campaigns and model setup used to conduct our study. The two field campaigns were conducted independently of each other and with different research foci (cloud and boundary layer research, respectively) at two different locations (hilly terrain in the Swiss Alpine foreland and highly complex terrain in the Austrian Alps, respectively). We took advantage of the availability of observational data obtained from a broad range of instruments employed in both campaigns to validate our model. Table 1 gives an overview of the field campaigns, the instruments used in this study, and the cases simulated here.

2.1 Field campaigns

2.1.1 CLOUDLAB

The CLOUDLAB project used glaciogenic cloud seeding to study ice processes in supercooled low-stratus clouds (Henneberger et al., 2023; Miller et al., 2024; Omanovic et al., 2024a). The field site is located at the edge of the Swiss Plateau on a prominent hill at 920 m a.m.s.l. surrounded by hilly terrain. It entailed three field campaigns (January–March 2022, December 2022–February 2023, and December 2023–February 2024), during which an extensive setup of remote sensing and meteorological instruments were present. A full list of the instruments can be found in Henneberger et al. (2023). For our analysis, we include an all-sky camera (FE9382-EHV-v2, Vivotek, snapshots (see Fig. 1) and videos (please find the video supplement in Omanovic et al., 2024b)), a microwave radiometer (HATPRO-G5, RPG) for continuous atmospheric temperature profiles, a ceilometer (CHM 15k, Lufft) for the aerosol layer height detection, and cloud products from CloudNET (Illingworth et al., 2007). The latter is software based on Python (Tukiainen et al., 2020), taking into account observations from cloud radars, lidar, a microwave radiometer, and model input from numerical weather prediction models to characterize clouds. This includes the determination of the liquid water content (LWC) and ice water content (IWC), both of which are used to validate our model simulations, as well as the liquid and ice water path (LWP and IWP, respectively).

2.1.2 CROSSINN

The Cross-valley flow in the Inn Valley investigated by dual-Doppler lidar measurements (CROSSINN) campaign took place in the summer and autumn of 2019 in the Inn Valley, Austria, with a focus on thermally induced circulations and the mountain boundary layer. The Inn Valley is a major east-to-west-oriented Alpine valley with a peak-to-peak distance of 10 km, while the valley bottom extends 5 km at our location of interest, located around 30 km east of the city of Innsbruck (Fig. 1a). An overview over the campaign and the employed instruments can be found in Adler et al. (2021b). All instruments (Table 1) mentioned in the next paragraph are located on the valley floor, together with the so-called i-Box turbulence flux towers (Rotach et al., 2017). In our study focusing on clouds, we use observations from a ceilometer (CHM 15k; Lufft) for a proxy to cloud base, a microwave radiometer (HATPRO-G4; Raymetrics) for LWP observations, and radiosonde launches (every 3 h) for vertical profiles of temperature and wind. All-sky images and animations are obtained from a visible and infrared camera (MX-S15D; Mobotix AG)

2.2 Model setup and simulations

We employed the numerical weather prediction model ICON (v2.6.6) (Zängl et al., 2015) in the limited-area mode with varying horizontal resolutions (from 1 km down to 65 m; see Fig. 1a) and 80 vertical levels, with the model top at 22 km (see Fig. A1). A recent study by Schmidt et al. (2024) showed that for varying vertical resolutions (on a global storm-resolving scale, i.e., 5 km), no convergence could be found for the microphysical properties. Also, tests conducted with the model setup (but for different case studies) showed no improvement in the cloud representation or temperature inversions (Schöni, 2023) with increasing verti-

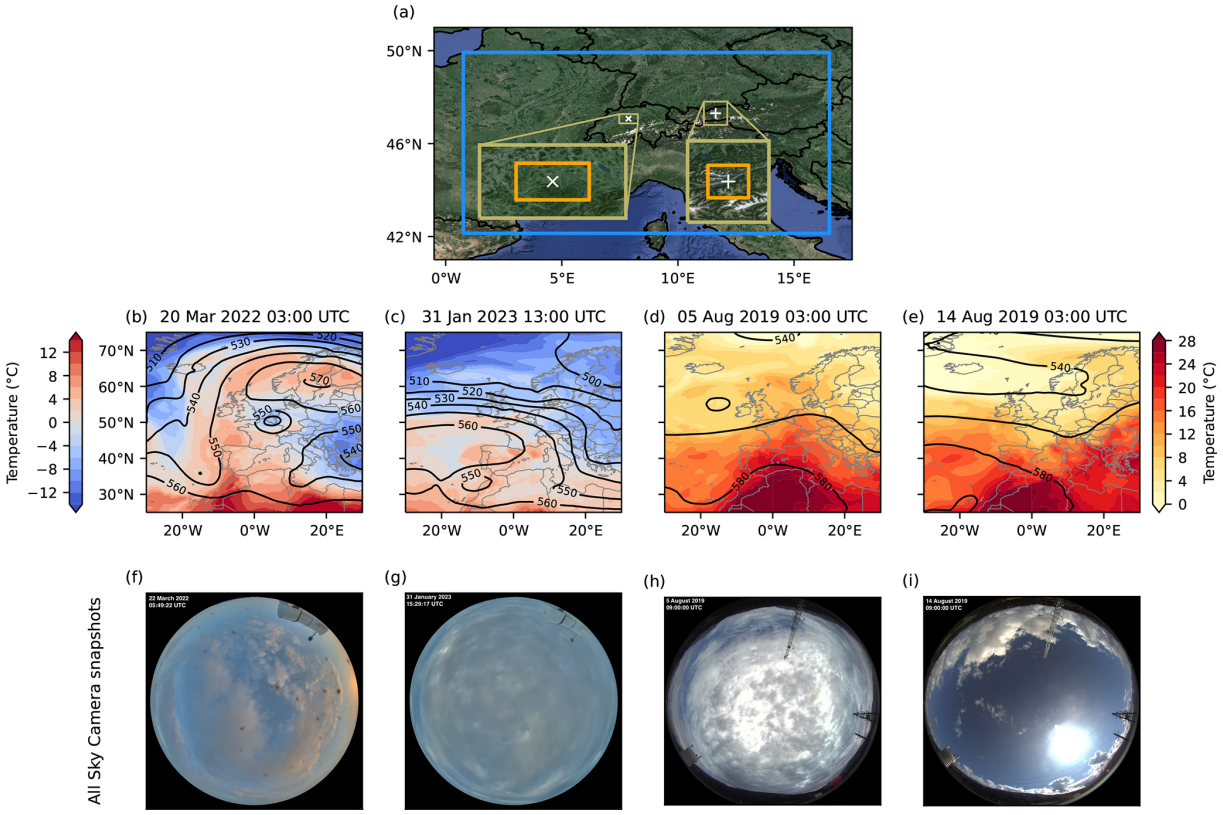

Figure 1. The first row **(a)** shows the model setup, with "x" and "+" denoting the field sites of CLOUDLAB and CROSSINN, respectively. The two model domains of interest in this study are the blue ($\Delta x = 1$ km) and the orange boxes ($\Delta x = 65$ m), with the olive green box ($\Delta x = 125$ m) denoting the domain in which the 65 m simulation was nested. The map is taken from Google satellite images (© Google Maps). The second row **(b–e)** shows the large-scale weather situation for our four case studies based on ERA5 data (Hersbach et al., 2020), with the coloring representing the temperature (°C) at 850 hPa and the black contours showing the geopotential height (decameter) at 500 hPa. The last row **(f–i)** is a collection of snapshots from the all-sky cameras located at the two field sites, where each snapshot corresponds to one case study and shows a typical cloud situation for that day (time stamp in the upper-left corner). Panels **(b)**, **(c)**, **(f)**, and **(g)** (left-hand side) are the case studies for the CLOUDLAB field site, while the others (right-hand side) are for the CROSSINN field site. Panel **(f)** shows that dirt fragments (dark dots) were present on the all-sky camera lens.

cal resolution. Hence, we decided to only vary the horizontal resolution and keep the vertical resolution the same as it is used in the operational model setup by the Swiss Federal Office of Meteorology (MeteoSwiss). While the 1 km domain covers the Alps, we have two smaller domains for our two separate measurement locations with $\Delta x = 65$ m; both are nested in a larger $\Delta x = 125$ m domain. Both the 1 km and 125 m domains receive their initial and boundary conditions (hourly update) from the COSMO-1 analysis (Schmidli et al., 2018) generated by MeteoSwiss. A brief comparison of cloud representation in the COSMO-1 analysis and the resulting ICON runs ($\Delta x = 1$ km) revealed realistic cloud patterns in the COSMO analysis data and no large discrepancies with ICON. This setup is similar to Schemann et al. (2020) and Schemann and Ebell (2020), who found that constraining the model with a driving model (COSMO-1) yields an improved model performance when compared to observations of cloud properties. Furthermore, the impact of the driving model on the nested model should be minimal compared to the internal model variability and errors (Davies, 2014). The boundary conditions for the innermost domain (65 m) are updated every 30 min. The model time steps are 10, 1, and 0.5 s, respectively. We use high-resolution static input data for all domains, we employ the ASTER dataset with $\Delta x = 30$ m (NASA/METI/AIST/Japan Spacesystems and US/Japan ASTER Science Team, 2009) for topography; for land use, we use the CORINE dataset (European Environmental Agency, 2017); and for soil properties, we use the Harmonized World Soil Database (FAO/IIASA/ISSCAS/JRC, 2012). Radiation is parameterized with the ecRad scheme after Hogan and Bozzo (2018). Since our model setup operates at $\Delta x = 1$ km and below, both the deep- and shallow-convection schemes are switched off. Mixing is achieved with a Smagorinsky-type (Lilly, 1962; Smagorinsky, 1963) turbulence scheme implemented by Dipankar et al. (2015) and frequently used in ICON simulations in the

kilometric and hectometric range (e.g., Heinze et al., 2017a; Hohenegger et al., 2023; Goger and Dipankar, 2024). The turbulence scheme is coupled to a surface exchange scheme, after Louis (1979), and the soil model TERRA_ML with eight soil levels (Schulz and Vogel, 2020).

Given that we investigate the model performance in terms of cloud microphysics schemes, we conduct simulations with the one-moment microphysics (1M; Seifert, 2006; Doms et al., 2021) and the two-moment microphysics scheme (2M; Seifert and Beheng, 2006) for all resolutions. The former tracks only mass mixing ratios for cloud droplets, ice crystals, snow, rain, and graupel, while the latter also tracks the number of mixing ratios for the same hydrometeors and also hail. Often these parameterizations are based on laboratory experiments or simplified theoretical concepts (Pruppacher and Klett, 1978). We provide here a short description of the processes relevant for our analysis and their representation in the bulk microphysics.

- *Cloud droplet activation*. The first and foremost process is cloud droplet activation, which requires the hygroscopic growth of aerosols that act as cloud condensation nuclei (CCN). A cloud droplet is activated once it experiences spontaneous growth after passing a critical supersaturation with respect to water (generated through updrafts, i.e., adiabatic cooling of air) and critical size (Lohmann et al., 2016). In 1M, the cloud droplet number concentration is prescribed, given that only mass mixing ratios are predicted and "activation", i.e., the prescribed concentration, only occurs when supersaturated conditions are met (Doms et al., 2021). The prescribed cloud droplet number concentration is $200\,\mathrm{cm}^{-3}$. Hence, no hygroscopic growth of aerosol particles occurs. In the case of 2M, where both the mass and number mixing ratios are prognostic, the cloud droplet number concentrations are calculated based on the updraft (measure for supersaturation) and a prescribed number of CCN ($250\,\mathrm{cm}^{-3}$), and their radius and a constant parameter account for hygroscopicity. For computational efficiency, this is achieved with so-called lookup tables that contain pre-calculated values for the activated cloud droplet number concentrations based on a matrix of the aforementioned parameters (Walko et al., 1995; Feingold et al., 1998; Seifert and Beheng, 2006). This cloud process already highlights the different levels of sophistication between the two bulk schemes.

- *Saturation adjustment*. We furthermore want to highlight a method that is introduced in the model to simplify the growth and evaporation of cloud droplets. Instead of following a mass growth equation for cloud droplets (Lohmann et al., 2016), so-called saturation adjustments are performed before and after the cloud microphysics. In the saturation adjustment, the water vapor saturation pressure is calculated in the current grid box, and according to the water vapor deficit/surplus, cloud droplets will evaporate/grow (through condensation), respectively, to achieve saturation. This only applies to the liquid phase; hence, ice crystals can experience supersaturation with respect to ice.

- *Ice nucleation*. Another fundamental process is the formation of ice crystals in clouds, which can occur in mixed-phase clouds (both liquid and ice phase present) or ice clouds (i.e., cirrus clouds). In ice clouds, we find the process called homogeneous nucleation, which is the freezing of a solution droplets in the atmosphere and only occurs at temperatures below $-38\,^{\circ}\mathrm{C}$. For the temperature regime between -38 and $0\,^{\circ}\mathrm{C}$, aerosols (ice nucleating particles, INPs) are again required to help form ice crystals (heterogeneous nucleation) (Lohmann et al., 2016). A broad range of aerosols can act as INPs (Kanji et al., 2017), with the most prominent and abundant being dust particles. In models with 1M, the ice crystal number concentrations are prescribed as a function of temperature, while with 2M the dedicated parameterizations for ice nucleation with prescribed aerosols are available. Most often a parameterization for dust particles only is implemented (e.g., Phillips et al., 2008; DeMott et al., 2015; Hande et al., 2015), which is a deterministic equation with a temperature dependence and a freezing onset temperature. We decided to follow the ice nucleation scheme by Phillips et al. (2008) for dust particles, which can form ice at temperatures below $-8,^{\circ}\mathrm{C}$.

- *Hydrometeor growth*. In both bulk schemes, the hydrometeors can collide and coalesce (cloud droplets), respectively; aggregate (ice crystals) and thus form larger particles, such as raindrops and snow; and sediment (and possibly precipitate) if they reach larger sizes. All of which require additional parameterizations (Doms et al., 2021; Seifert and Beheng, 2006). Another process we want to highlight is the Wegener–Bergeron–Findeisen process (Wegener, 1911; Bergeron, 1935; Findeisen, 1938), which takes place when both the liquid and ice phase are present. It describes the growth of ice crystals through water vapor deposition, while cloud droplets evaporate due to the reduction in supersaturation. In this way, cloud droplets act as a water vapor source for ice crystals to grow (Korolev and Mazin, 2003; Korolev, 2007). Through this process, mixed-phase clouds can be glaciated; i.e., the liquid phase evaporates and only the ice phase is left. It is known that the Wegener–Bergeron–Findeisen process is crucial for the cloud lifetime and its radiative effects, and weather and climate models struggle to accurately represent it (Liu et al., 2011; Kay et al., 2016; Klaus et al., 2016; McIlhattan et al., 2017; Kretzschmar et al., 2019; Huang et al., 2021; Omanovic et al., 2024a).

Table 2. The naming convention used in this study for the single studies. We differentiate between the two field campaigns by their topography (hilly vs. complex) and further distinguish between the horizontal resolutions of $\Delta x = 1$ km and $\Delta x = 65$ m and the employed microphysics scheme (one-moment (1M) and two-moment (2M) microphysics scheme).

Field campaign	CLOUDLAB (hilly terrain)				CROSSINN (complex terrain)			
Resolution	1 km		65 m		1 km		65 m	
Microphysics scheme	1M	2M	1M	2M	1M	2M	1M	2M
Simulation name	HT1 1M	HT1 2M	HT65 1M	HT65 2M	CT1 1M	CT1 2M	CT65 1M	CT65 2M

By combining the two field campaigns, we can conduct a model validation study in hilly (CLOUDLAB) and complex (CROSSINN) terrain. For clarity, we named the performed simulations after their topography, resolution, and the microphysics scheme; i.e., "HT1 1M" stands for a hilly terrain simulation with $\Delta x = 1$ km and the one-moment microphysics scheme, while "CT65 2M" describes a complex terrain simulation with $\Delta x = 65$ m and the two-moment microphysics scheme (see Table 2). For model validation, we use the so-called `meteogram` output as in Schemann et al. (2020), a single-point data output stream at the frequency of the model time step (10 s for $\Delta x = 1$ km and 0.5 s for $\Delta x = 65$ m, respectively). To ensure the correct spatial representation, we take a spatial average of five meteograms, with one being at the location of the field site and the other four being equally distributed in a 100 m radius around the field site. For comparing the cloud characteristics, we apply a threshold value of 0.01 g m^{-3} for liquid and ice water content to the observations and simulations to only consider in-cloud values.

2.3 Case study selection

The selection of the case studies was (1) limited by the operation times of the field campaigns, (2) the availability of observational data, and (3) the occurrence of non-precipitating clouds. The latter was chosen because some observational instruments cannot measure reliably during precipitation events (e.g., microwave radiometer) or because the reflectivity signal of remote sensing instruments is saturated (e.g., cloud radars). Hence, we decided to focus on the following cloud types, namely altocumulus (see Fig. 1f, h, and i) and stratocumulus (see Fig. 1g) clouds. We identified the cloud types based on their height and the aerosol layer height, which serves as an indicator for the boundary layer height (see Figs. 3a, c and 7a, c). If the cloud was above the aerosol layer height, we classified it as an altocumulus cloud; otherwise, it was a stratocumulus cloud.

3 Results

3.1 Hilly terrain (HT)

In the following, we discuss the two case studies for hilly terrain (CLOUDLAB field site), first by comparing the cloud cover extent for HT1 and HT65 1M/2M and then looking at the cloud characteristics, such as liquid and ice water content (LWC and IWC, respectively). While we do not have any observations of the cloud droplet and ice crystal number concentrations, we include a discussion in Sect. 3.3 (respective figures for other cases are in Appendix D) regarding the diagnosed (1M) and predicted (2M) number concentrations for all cases in hilly and complex terrain.

3.1.1 20 March 2022: altocumulus clouds

The 20 March 2022 case study was characterized by weak westerly winds due to a weak low-pressure system northwest of Switzerland (see Fig. 1b) which led to the formation of altocumulus clouds during the nighttime before dissolving in the morning hours (see the video supplement in Omanovic et al., 2024b, and Fig. 3a and c). We first compare the cloud cover extent for HT1 and HT65 in the 1M and 2M configuration (Fig. 2) for the closest time step to the all-sky camera snapshot (see Fig. 1f). The cloud cover is diagnosed based on the present LWC and IWC in the middle of the simulated cloud and ranges from 0 % to 100 %. Both resolutions simulate patchy clouds passing through the model domain, with HT1 showing larger and more coherent cloud structures, which is to be expected given the resolution. In general, HT65 predicts a larger fractional cloud cover and a longer-lived cloud (see the video supplement in Omanovic et al., 2024b). Looking at the normalized frequency distribution (Fig. B1), we do not see large differences between the two resolutions with respect to their cloud cover distribution. For the comparison between 1M and 2M, we see no clear signal for both resolutions but rather a spatial shift (HT1) or smaller extent of the cloud (HT65), with the largest differences at the cloud edges, which may be due to differences in turbulent mixing and also numerical diffusion. The similarity between the model setups is also notable in Fig. B1, where both configurations are fairly similar.

Next, we look at the liquid and ice water content and path (LWC/LWP and IWC/IWP, respectively) in the observations

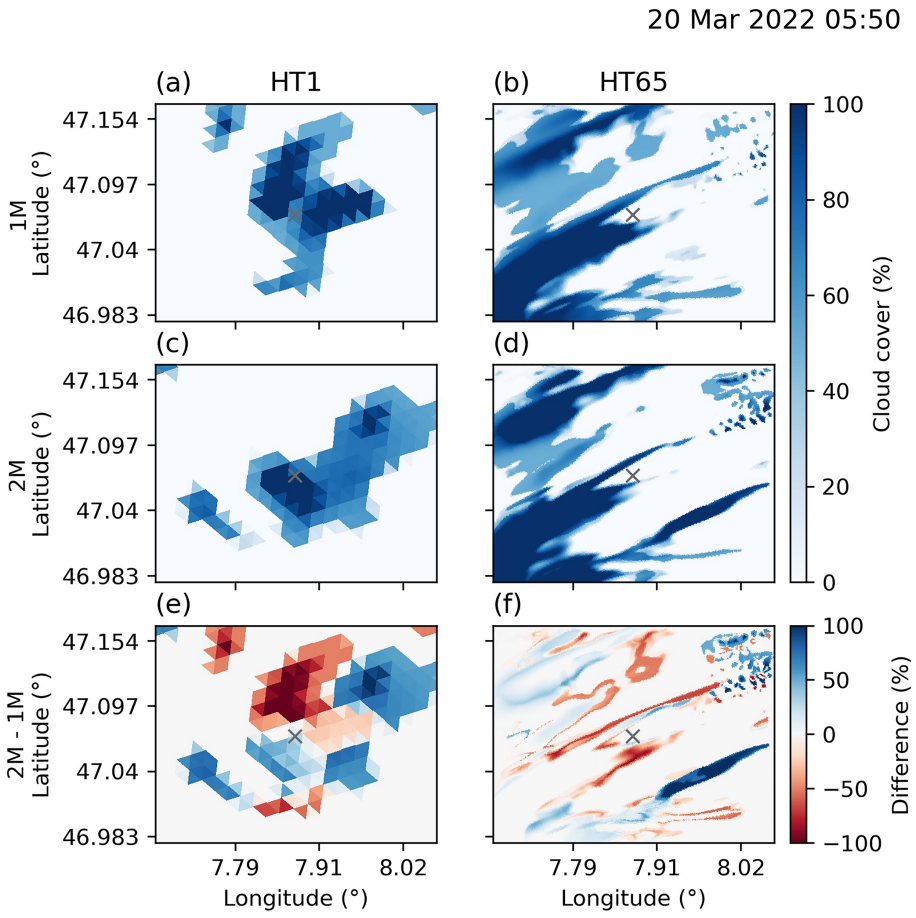

Figure 2. Comparison of fractional cloud cover (%) at ∼ 2500 m a.g.l. (above ground level) for the case study on 20 March 2022 at 05:50 UTC (the closest time step to the all-sky camera snapshot in Fig. 1f) for HT1 **(a, c, e)** and HT65 **(b, d, f)** in the 1M **(a, b)** and 2M **(c, d)** configurations and their difference (2M–1M; **e, f**). The "x" symbol marks the CLOUDLAB field site. The domain of HT1 was enlarged to show the same extent as HT65.

and the model simulations (Fig. 3). From the observations, we see that a cloud appears shortly after 03:00 UTC and thickens with time. The LWC occurs only sporadically, with values of up to 15 g m^{-3}, while the rest of the cloud is attributed to the ice phase by CloudNET (Fig. 3c). Given the cold temperatures at cloud height (Fig. B2; ∼ −10 °C) ice crystals can form by heterogeneous nucleation on aerosols (Kanji et al., 2017) and lead to a full glaciation of the cloud due to the favored growth of ice crystals in subzero temperatures compared to cloud droplets due to their difference in the water vapor saturation pressure (i.e., the Wegener–Bergeron–Findeisen process).

When looking at the results from HT1 1M, we see that the model simulates a short-lived ice cloud (LWC/LWP are close to zero) around the time of the observed cloud (Fig. 3e). HT1 2M, however, simulates a liquid layer above 3000 m (Fig. 3i), which persists for several hours. The origin of this liquid layer may stem from the positive vertical velocities (i.e., updrafts) in that region that are more prominent in 2M than in 1M (see Fig. 4g). We see strong differences between HT1 and HT65. For the latter, 1M and 2M are able to simulate an ice cloud with a time delay of about 1 h and two distinct clusters as observed by the remote sensing instruments (Fig. 3c, h and l), while 2M shows a higher IWC/IWP than 1M, which also impacts the vertical structure of temperature (Fig. B2h). This difference may come from slightly higher updrafts inside the cloud, thus invigorating ice formation (see Fig. 4h). In both configurations, LWC is very low and occurs only sporadically (Fig. 3f and j). While there is qualitative agreement between the model simulations and observations, we see a large discrepancy in the total amount of liquid exemplified by the LWP shown in Fig. 3b and by the mean and the standard deviation in LWC listed in Table 3. The model underestimates the LWC by a factor of 3, while the LWP agrees better. The LWP measurements shown in Table 3 are based on a microwave radiometer. The LWC is based on the CloudNET algorithm, which combines several instruments and model data to classify the cloud. In this case,

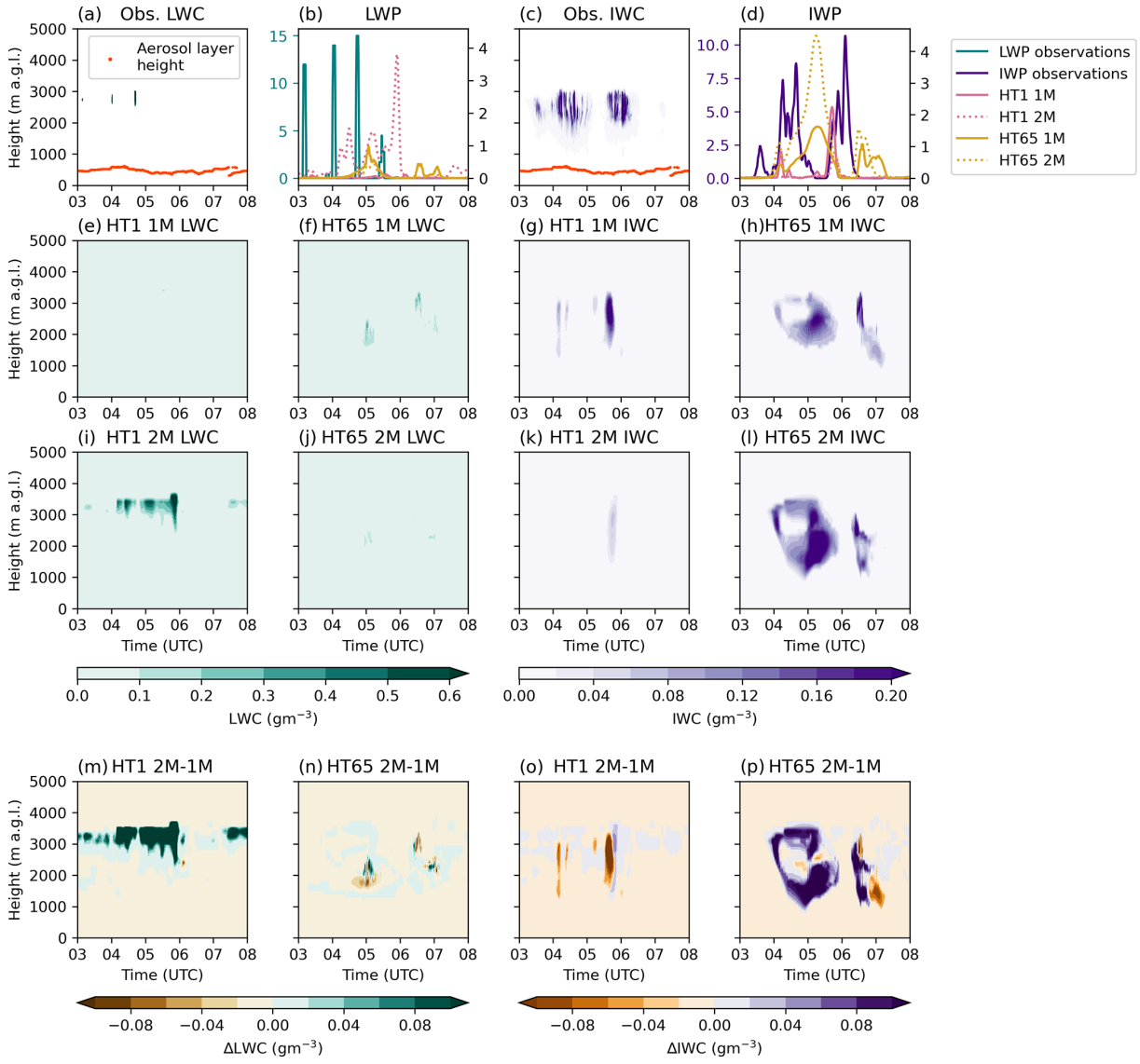

Figure 3. Overview of cloud characteristics for the case study on 20 March 2022. Panels **(a)** and **(c)** show the liquid water content (LWC; g m^{-3}) and ice water content (IWC; g m^{-3}), based on the algorithm by CloudNET with the aerosol layer height (orange dots) serving as a proxy for the boundary layer height. Panels **(e)–(l)** show the model responses for LWC and IWC for both resolutions (HT1 and HT65) and both bulk microphysics schemes (1M and 2M). Panels **(b)** and **(d)** show the observed (left *y* axis) and the simulated (right *y* axis) LWP and IWP (g m^{-2}), respectively.

the classification as a liquid cloud occurs only sporadically, leading to a very high LWC given the measured LWP. Hence, the interpretation of the LWC should be handled with care. For the ice phase, the agreement between the observations and simulations is better (see Table 3), except for HT 2M, which strongly underestimates the IWC and IWP.

Figure 5 (for the second case study, see Appendix D and Fig. D1; for the simulations in complex terrain, see Fig. D2) shows the temporal evolution of the cloud droplet and ice crystal number concentrations (CDNCs and ICNCs, respectively) for both resolutions and both microphysics schemes for the hilly terrain case studies. As mentioned, the CDNCs are prescribed in 1M (= 200 cm^{-3}) as soon as a cloud forms. In the model, the CDNC is only used for calculating the collection kernels between the droplets, and it does not change over time. In the figures, the markers are only set for illustrative purposes and highlight when the LWC exceeded 0.01 g m^{-3} in 1M simulations. In 2M, CDNCs are predicted, and thus, they change with time and depend on the cloud droplet activation and removal due to collision processes (see Sect. 2). In both schemes, the collision and coalescence rate of cloud droplets (i.e., autoconversion) may be low. In 1M, the high CDNC and low LWC lead to small cloud droplets that limit collisions, and in 2M, low CDNC and low LWC

Table 3. Mean and standard deviation of liquid and ice water content ($g\,m^{-3}$; LWC and IWC, respectively) averaged over the entire cloud and liquid and ice water path ($g\,m^{-2}$; LWP and IWP, respectively) for both resolutions and cloud microphysics schemes for the case on 20 March 2022 shown in Fig. 3. Only grid points with a LWC and IWC $> 0.01\,g\,m^{-3}$ were included. Based on these values, the LWP and IWP were calculated.

	Observation	HT1		HT65	
		1M	2M	1M	2M
LWC	2.49 ± 3.24	0.074 ± 0.061	0.159 ± 0.146	0.053 ± 0.031	0.037 ± 0.022
LWP	0.17 ± 2.43	0.188 ± 0.293	0.483 ± 0.671	0.172 ± 0.138	0.183 ± 0.133
IWC	0.07 ± 0.07	0.071 ± 0.055	0.037 ± 0.014	0.059 ± 0.044	0.099 ± 0.084
IWP	0.31 ± 1.30	0.482 ± 0.595	0.268 ± 0.166	0.345 ± 0.356	0.363 ± 0.847

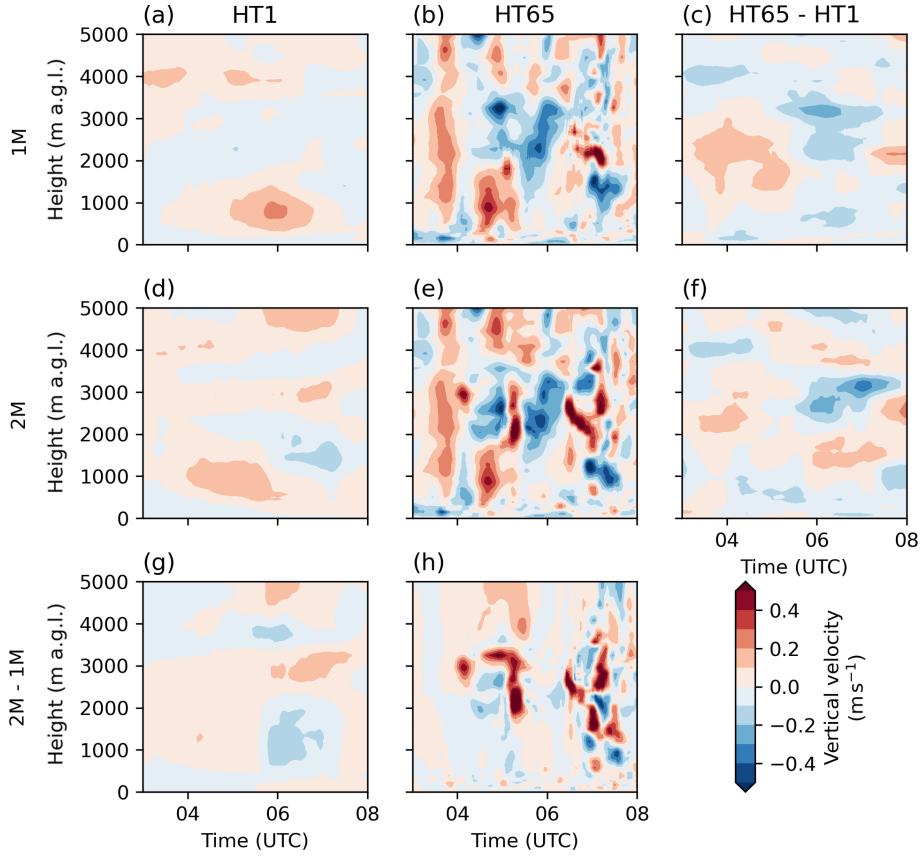

Figure 4. Hovmöller diagrams for vertical velocity ($m\,s^{-1}$) averaged over 10 min for HT1 and HT65 with 1M and 2M, respectively, for 20 March 2022. The last column shows the differences between the resolutions (HT65–HT1), where HT65 was averaged over a running mean of 10 s to have the same time frequency as HT1. The last row shows the differences between 2M–1M for both HT1 and HT65.

also yield small autoconversion rates. The two microphysics schemes differ strongly in the CDNC, with the prescribed concentration in 1M probably being a better estimate for the CDNC for a continental cloud, while 2M predicts rather low concentrations. This could be a consequence of interactions with the ice phase, where at subzero temperatures, the ice phase is the favored state, and thus ice crystals will form and grow at the expense of evaporating cloud droplets. One hypothesis is that this balance in the model is more on the side of the ice crystals. This is further supported by the strong underestimation of the LWC/LWP in the simulations. For ICNCs, we see that 1M strongly underestimates it, which may arise from the equation for ICNCs from Cooper (1986), where at temperatures around −10 °C, the ICNC activity is underestimated. For 2M, we see that a realistic ICNC is simulated only for the HT65 simulation, with concentrations maximizing at $0.1\,cm^{-3}$, while for HT1, ICNC is by almost 3 orders of magnitudes too low, so also almost no IWC/IWP was simulated. Hence, the CDNC is strongly underestimated in 2M simulations, which may come from the balance between

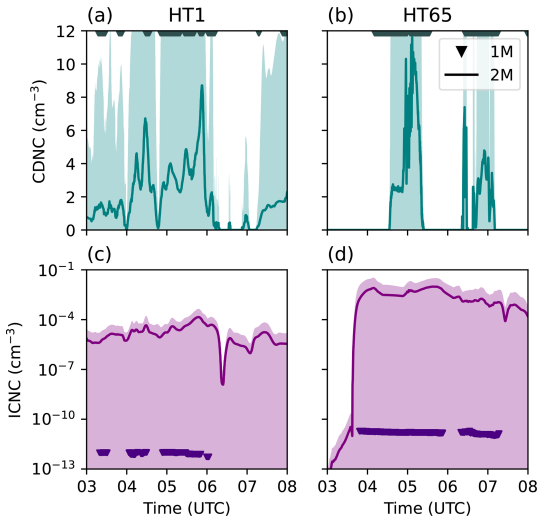

Figure 5. Simulated cloud droplet **(a, b)** and ice crystal **(c, d)** number concentrations (CDNCs and ICNCs, respectively) for 20 March 2022 for both resolutions (HT1 and HT65, **a/c** and **b/d**, respectively). The number concentrations from 1M are shown as markers whenever there is a cloud present. In 1M, CDNC = 200 cm^{-3} (prescribed; markers only for indicating cloudy conditions), while ICNC is calculated as a function of temperature, following Cooper (1986) (diagnosed). The predicted quantities from 2M are shown as means (solid lines) ± standard deviations (shading).

the liquid and ice phase. This is an issue that weather and climate models struggle with (Liu et al., 2011; Kay et al., 2016; Klaus et al., 2016; McIlhattan et al., 2017; Kretzschmar et al., 2019; Huang et al., 2021; Omanovic et al., 2024a), so we see a more realistic simulation of ICNC than for 1M. For the complex terrain case studies in summer, we only investigate CDNC (Fig. D2). The concentrations are slightly higher (a factor of 2) than for the HT simulations, but this is probably still an underestimation as higher CDNC can be expected over land (Lohmann et al., 2016).

3.1.2 31 January 2023: stratocumulus clouds

The second case we investigate is stratocumulus clouds that formed in the afternoon of 31 January 2023. The weather was characterized by northwesterly winds (see Fig. 1c). The cloud lived for several hours, and at times, ice crystals sedimented towards the ground, causing a large vertical extent of the cloud (see Fig. 7a and c).

We again first compare the cloud covers at 2500 m for HT1 and HT65 in Fig. 6, which shows the closest time step to the all-sky camera snapshot in Fig. 1g. While we see a full-cloud layer in the snapshot, both model resolutions simulate a more patchy cloud, with HT65 showing clouds in the form of streaks, and HT1 showing more grouped-together clouds (see the video supplement in Omanovic et al., 2024b). Both resolutions cannot reproduce the observed cloud conditions. In terms of the performance of the cloud microphysics scheme, we see a very similar behavior to that in the previous case study (20 March 2022), where the strongest differences between 1M and 2M occur at the cloud edges (due to differences in turbulent mixing and/or numerical diffusion), which appears to be more extreme in the case of HT1 given the coarser resolution. When looking at the normalized frequency distribution, we cannot distinguish any large differences (Fig. B3). This points to a more stochastic nature of the schemes, than to systematic changes caused by the choice of scheme.

Figure 7 shows the LWC/LWP and IWC/IWP for the observations and model simulations. We see a longer-lived cloud than in the previous case, with a liquid layer that descends over time from 3000 to 2000 m (Fig. 7a). We also see that the cloud produced very light precipitation (long purple streaks reaching the ground and increasing in the aerosol layer height in Fig. 7c). HT1 1M and HT1 2M simulate a weaker liquid layer, whereas the liquid layer increases in height with time before it dissolves too early (Fig. 7e and i), and in the early night a liquid layer forms again. 1M and 2M have similar LWPs during the lifetime of the cloud, with 2M showing slightly higher values for the early afternoon hours. Similar to the other case study, LWP is underestimated in the model by a factor of 2 (Fig. 7b). While CloudNET classified parts of the cloud to be ice, the model barely simulates any ice (Fig. 7g and k), further highlighted by the very low IWP in Fig. 7d. We see a different picture for the case of HT65 (Fig. 7f, j, h, and l). We barely have any LWC present in 1M or 2M (Fig. 7f and j and Table 4). Both configurations simulate some ice clouds in the early afternoon, where 2M again shows a higher IWC/IWP than 1M. However, for both schemes, the cloud is shorter-lived than in the observations failing to reproduce the longevity of the observed cloud. Including the vertical velocity in our analysis (Fig. 8), we see that HT65 in general has stronger vertical velocities than HT1 (±0.3 m s^{-1}). This may lead to an invigorated ice formation as seen in both configurations, namely 1M and 2M.

3.2 Complex terrain (CT)

As mentioned in the description of the observations, the CROSSINN campaign's focus was not on cloud observations. Nevertheless, vertical profiles from radiosondes, backscatter from a ceilometer, an all-sky camera, and LWP observations from the HATPRO radiometer can be utilized for our model validation study. Since we are validating summertime case studies, the clouds in the CT simulations mostly consist of water, and only liquid water content (LWC) is compared. Observations and simulations of vertical profiles of temperature (Fig. C1) suggest that the 0° line is above 3000 m a.g.l. (5 August 2019) and 2000 m a.g.l. (14 August 2019), respectively. Given that ice clouds form at temperatures below −8 °C (Phillips et al., 2008), we assume that the clouds in the two following case studies only consist of

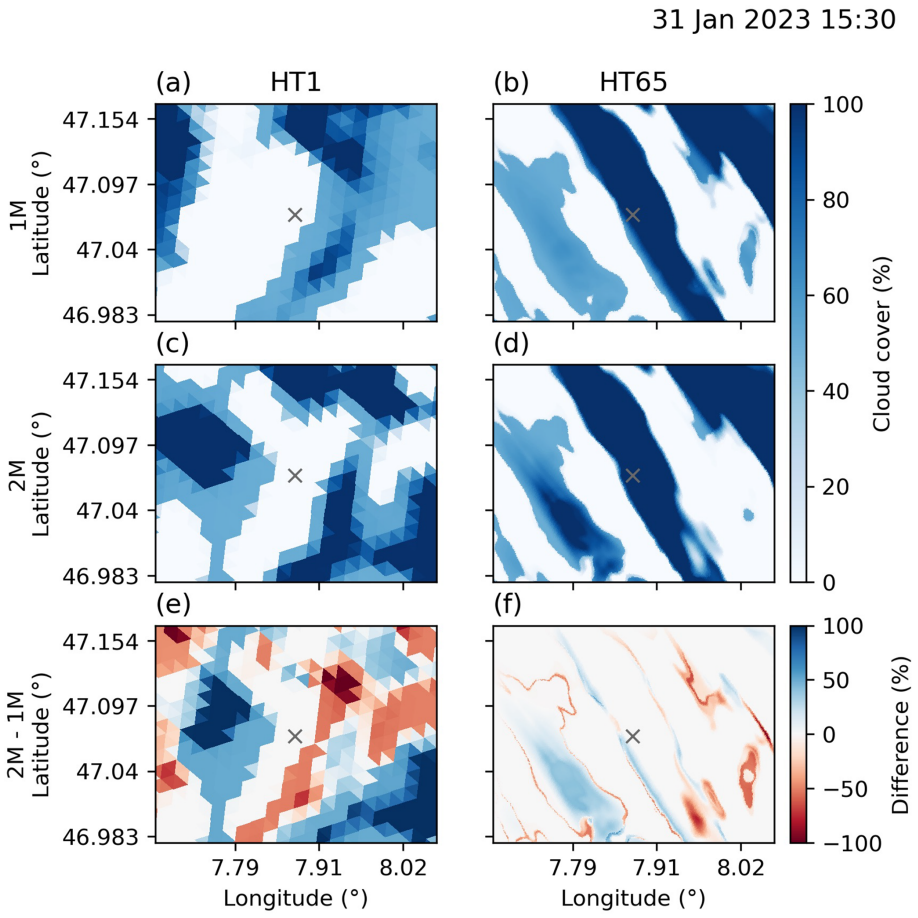

Figure 6. Comparison of fractional cloud cover (%) at ∼ 2500 m a.g.l. for the case study on 31 January 2031 at 15:30 UTC (closest time step to all-sky camera snapshot in Fig. 1g) for HT1 **(a, c, e)** and HT65 **(b, d, f)** in the 1M **(a, b)** and 2M **(c, d)** configurations and their difference (2M–1M, **e, f**). The "x" symbol marks the CLOUDLAB field site. The domain of HT1 was enlarged to show the same area as HT65.

Table 4. Mean and standard deviation of liquid and ice water content (in $g\,m^{-3}$) (LWC and IWC, respectively) averaged over the entire cloud and liquid and ice water path (in $g\,m^{-2}$) (LWP and IWP, respectively) for both resolutions and both cloud microphysics schemes for the case on 31 January 2023 shown in Fig. 7. Only grid points with a LWC and IWC $> 0.01\,g\,m^{-3}$ were included. Based on these values, LWP and IWP were calculated.

	Observation	HT1		HT65	
		1M	2M	1M	2M
LWC	0.13 ± 0.19	0.145 ± 0.125	0.152 ± 0.141	0.023 ± 0.016	0.015 ± 0.003
LWP	0.55 ± 0.88	0.171 ± 0.189	0.446 ± 0.454	0.033 ± 0.022	0.018 ± 0.004
IWC	0.25 ± 0.43	0.035 ± 0.025	0.005 ± 0.001	0.036 ± 0.042	0.068 ± 0.057
IWP	1.46 ± 7.13	0.079 ± 0.102	0.005 ± 0.012	0.059 ± 0.143	0.156 ± 0.327

liquid water, and we hereby only analyze the liquid water content.

3.2.1 5 August 2019: altocumulus clouds

The date of 5 August 2019 was characterized by a high-pressure system over central Europe (Fig. 1d), suggesting a weak synoptic influence over the Alps. The Inn Valley was mostly dominated by low wind speeds below $4\,m\,s^{-1}$, with down-valley flows during the nighttime and up-valley flows during the daytime. The all-sky camera shot at 09:00 UTC in the Inn Valley suggests an altocumulus cloud layer covering the entire sky view, while the video animation (Omanovic et al., 2024b) suggests that this cloud layer persists, with occasional interruptions, for most of the day. The closest model time step to the all-sky camera snapshot shows large differ-

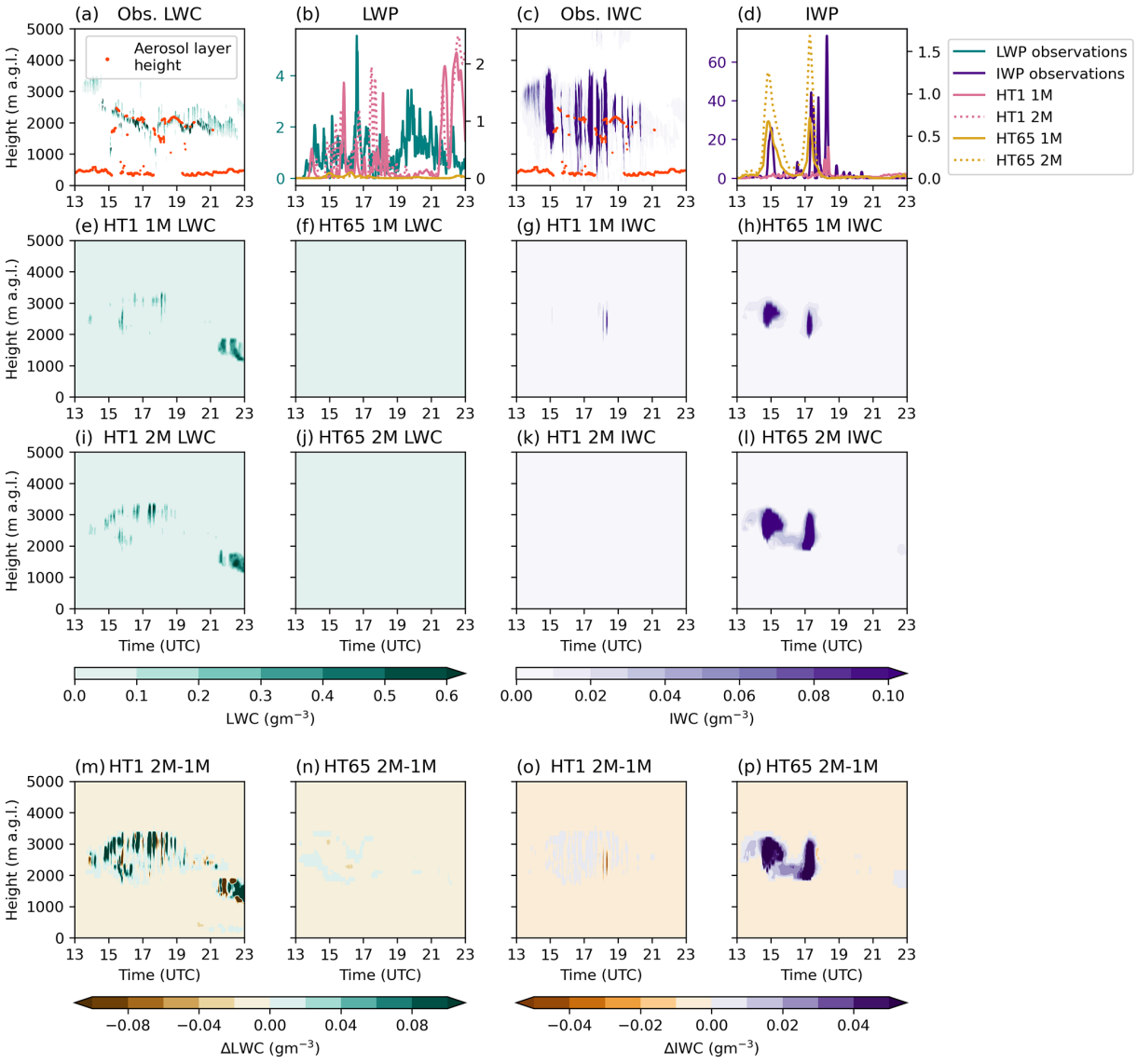

Figure 7. Overview of cloud characteristics for the case study on 31 January 2023. Panels **(a)** and **(c)** show the liquid water content (LWC; g m^{-3}) and ice water content (IWC; g m^{-3}) based on the algorithm by CloudNET, with the aerosol layer height (orange dots) serving as a proxy for the boundary layer height. Panels **(e)–(l)** show the model responses for LWC and IWC for both resolutions (HT1 and HT65) and both bulk microphysics schemes (1M and 2M). Panels **(b)** and **(d)** show the observed (left *y* axis) and the simulated (right *y* axis) LWP and IWP (g m^{-2}), respectively.

ences between the simulations and the observations (Fig. 9); at ≈ 4000 m above ground level (a.g.l.), the kilometric CT1 simulations show a patchy cloud cover over our area of interest. The cloud cover structure does not follow the underlying topography, mostly because these high clouds are already located above the highest peaks in the surroundings (above ≈ 3500 m a.m.s.l.). Interestingly, due to the patchiness of the cloud cover, there are no simulated clouds above our area of interest, which is the valley floor. The 2M scheme simulates thicker cloud cover than the 1M run. The CT65 simulations suggest a more continuous cloud layer at ≈ 4000 m a.g.l., covering most of our area of interest. We note here that this "patchiness" will also affect our interpretation of the model results in the next few paragraphs. As in the CT1 simulations, there is no clear signal as to whether the 1M scheme or the 2M scheme simulate "more" or "fewer" clouds (Fig. C2). The ceilometer observations from the valley floor (Fig. 10a) show a cloud-free night (00:00–02:00 UTC) in the first hours. After 03:00 UTC, a cloud layer with a cloud base height of around 400 m a.g.l. develops and remains persistent until 10:00 UTC (see the video supplement in Omanovic et al., 2024b). In the CT65 simulations (Fig. 10b and c), the simulated LWC suggests that there are no clouds present in the first few hours of simulations. Cloud development is de-

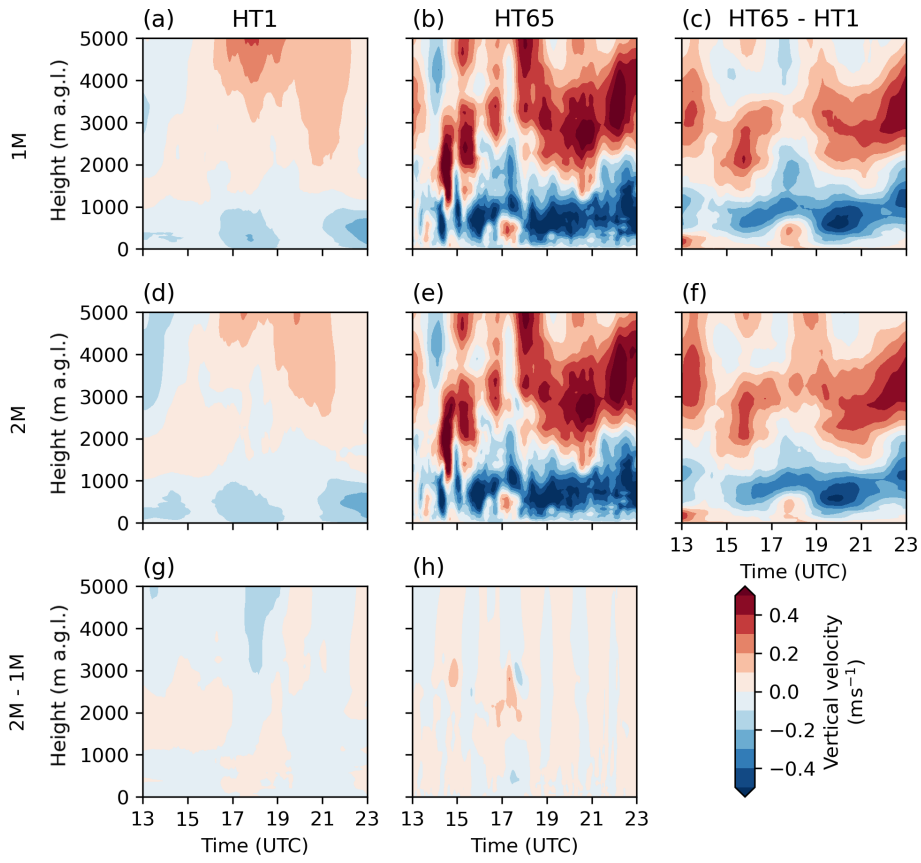

Figure 8. Hovmöller diagrams for vertical velocity (m s^{-1}) averaged over 10 min for HT1 and HT65 with 1M and 2M, respectively, for 31 January 2023. The last column shows the differences between the resolutions (HT65–HT1), where HT65 was averaged over a running mean of 10 s to have the same time frequency as HT1. The last row shows the differences between 2M–1M for both HT1 and HT65.

layed in the CT65 runs, and high clouds only form after 10:00 UTC. However, after 10:00 UTC, the CT65 simulates a realistic cloud structure with a similar cloud base height of 4000 m a.g.l., and the cloud remains persistent until the end of our time of interest (18:00 UTC). Changing the microphysics scheme has indeed an impact on simulated LWC; the 2M scheme simulated higher LWC amounts compared to the 1M run but still only after 10:00 UTC (Fig. 10d). This behavior is also visible in the simulated LWP (Fig. 10j), where the 2M scheme generally simulates higher LWP values of up to 12 g m^{-2}. Unfortunately, a HATPRO failure occurred between 12:00 and 17:00 UTC, so we cannot validate the simulations during this time period.

The CT1 simulations (Fig. 10e and f), however, show almost no clouds compared to the CT65 simulations. There are no relevant LWC amounts simulated for most of the time, with the only exception being for very short-lived (dissipation after several minutes of simulation time) clouds with LWC values below 0.04 g m^{-3} at around 12:00 UTC. The choice of the microphysics scheme has no positive impact on the simulation of clouds in the CT1 runs (Fig. 10g) at the valley floor. The LWP shows only small values before 12:00 UTC and at around 16:00 UTC but remains generally smaller than in the CT65 runs. A reason for the (almost) completely absent cloud formation can be found in the vertical velocity time series (Fig. 13). While the CT1 runs (Fig. 13f and j) are unable to resolve vertical motions, the CT65 runs (Fig. 13e and i) simulate continuous up- and downdrafts after 10:00 UTC, favoring cloud formation during this time period. The vertical profiles of observed and simulated potential temperature profiles at 15:00 UTC show a large discrepancy between the model and observations at 2000 m a.g.l. (Fig. 10h and i). Both simulations, CT65 and CT1, underestimate the horizontal wind speed, while simulating realistic potential temperature profiles. There is no clear indicator of why this happens, but 2000 m a.g.l. is approximately the crest height of the surrounding mountains, and it is possible that the model is unable to simulate the local flow structure at crest height accordingly, leading to unrealistic circulations affecting cloud formation. Still, it has to be pointed out that the CT65 simulation is able to produce a cloud cover over the valley because of basic small-scale flow features that are successfully simulated at sub-hectometric resolutions (Fig. 13e and f). Interestingly, as the video animation (Omanovic et al.,

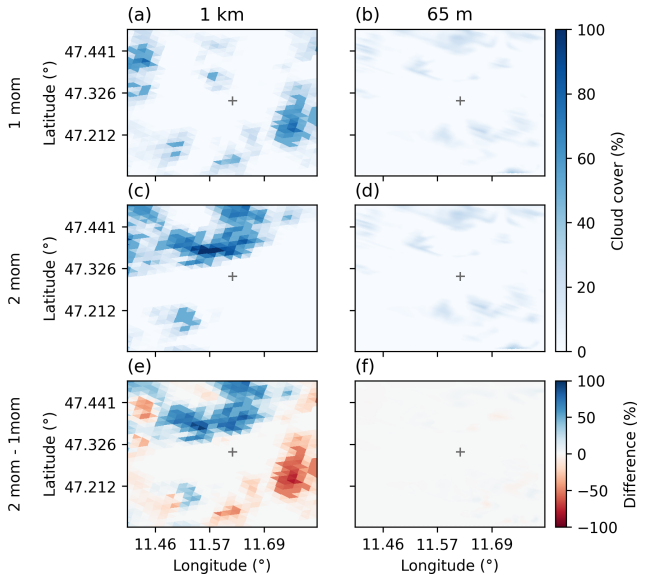

Figure 9. Comparison of cloud cover extent (%) at ∼ 4000 m a.g.l. for the case study on 5 August 2019 at 09:00 UTC (closest time step to all-sky camera snapshot in Fig. 1h) for CT1 **(a, c, e)** and HT65 **(b, d, f)** in the 1M **(a, b)** and 2M **(c, d)** configuration and their difference (2M–1M, **e, f**). The "+" symbol marks the CROSSINN field site. The domain of CT1 was enlarged to show the same area as HT65.

2024b) suggests, the CT1 simulation is able to produce altocumulus clouds that are mostly over the surrounding ridges but not over the valley itself. This is also evident in the histograms (Fig. C2), suggesting that both mesh sizes produce similar amounts of cloud cover independent of the microphysics scheme.

3.2.2 14 August 2019: altocumulus clouds

On 14 August 2019, the Alps were under the influence of westerly winds (see Fig. 1e). The local boundary layer in the Inn Valley was dominated by the formation of a thermally induced valley wind circulation (Lehner et al., 2019), resulting in down-valley flows during the nighttime and a distinct up-valley flow during the daytime. For this case study, we will mostly focus on the break-up of the low-lying nighttime stratus clouds and the following shallow-cumulus cloud formation. In the morning, a thick stratus layer with occasional precipitation was present in the valley. The stratus layer dissolved at around 06:00 UTC and throughout the rest of the day; mostly shallow altocumulus clouds were present over the valley and the surrounding mountains (see the video supplement in Omanovic et al., 2024b). A comparison with the simulations at 09:00 UTC shows that in the CT1 simulations, the valley itself is cloud-free, but over the mountains, clouds are visible in CT1 and CT65. In the CT1 runs, the 1M scheme simulates more clouds than the 2M scheme, although it is questionable whether the horizontal extent of the cumulus clouds over the mountains is realistic. In contrast, the CT65 simulations show small-scale altocumulus clouds scattered over the domain at the same time step, especially over the mountain slopes, and this is in better agreement with the all-sky camera observations (Fig. 1i). Both microphysics schemes simulate the scattered cumulus clouds, and major differences can only be seen in their location but not in their pattern.

The ceilometer observations at the valley floor (Fig. 12a) suggest a low-lying cloud layer during the nighttime, likely stratus or nimbostratus clouds, with occasional precipitation at 01:00 and 03:00 UTC. However, our time period of interest only starts at around 05:00 UTC (after sunrise), when the stratus cloud layer (at ≈ 2000 m a.g.l.) weakens and transforms to scattered altocumulus clouds (at ≈ 3000 m a.g.l.); this is especially visible in the intermittent backscatter of the ceilometer after 06:00 UTC. According to the observations, the cloud base height rises from around 2000 m a.g.l., together with a developing aerosol layer height, up to 3000 m a.g.l. during the daytime. A comparison with radiosonde observations and wind speeds suggests the development of a convective boundary layer, and the convection and up-slope flows lead to the formation of cumulus clouds over the surrounding mountain slopes and peaks and not over the valley floor itself. Still, the cumulus clouds are advected over the valley floor with the general up-valley flow, visible in the all-sky camera, leading to a transient cloud cover until around 14:00 UTC. After that, no clouds are recognizable in the ceilometer observations.

The CT65 simulation (Fig. 12b and c) suggests the presence of a low-stratus layer with a cloud base height of around 2000 m before 06:00 UTC, which is in agreement with the ceilometer observations. After the breakup of the low-stratus cloud layer at ≈ 06:00 UTC, the model simulates single smaller cumulus clouds with a cloud base height of around 3000 m a.g.l. over the valley floor, but compared to the ceilometer time series, the simulated cumulus clouds are fewer and weaker as well. When comparing the two microphysics schemes (Fig. 12d), the 2M scheme generally leads to larger LWC values ($+1.2\,\mathrm{g\,m^{-3}}$) in the 65M runs during the time of the low stratus. There is no clear signal for the daytime cumulus clouds because both microphysics produce occasional clouds; this is likely related to the very patchy (and transient) cloud cover also visible in Fig. 11. The simulated LWP (Fig. 12j) reveals that the CT65 runs simulate realistic values that are in agreement with the observations. However, there is a time shift in which the second maximum is simulated earlier (around 04:00 UTC), while the observations suggest that the second maximum appears later (06:00 UTC). The CT1 simulations suggest a low-lying cloud layer before 06:00 UTC as well (Fig. 12e and f), but the simulated cloud base layer lies clearly above 2000 m, suggesting a stratus layer with smaller vertical extent than in the CT65 runs. Furthermore, the stratus layer in the CT1 runs is less persistent than in the CT65 runs, and it is clearly visible in

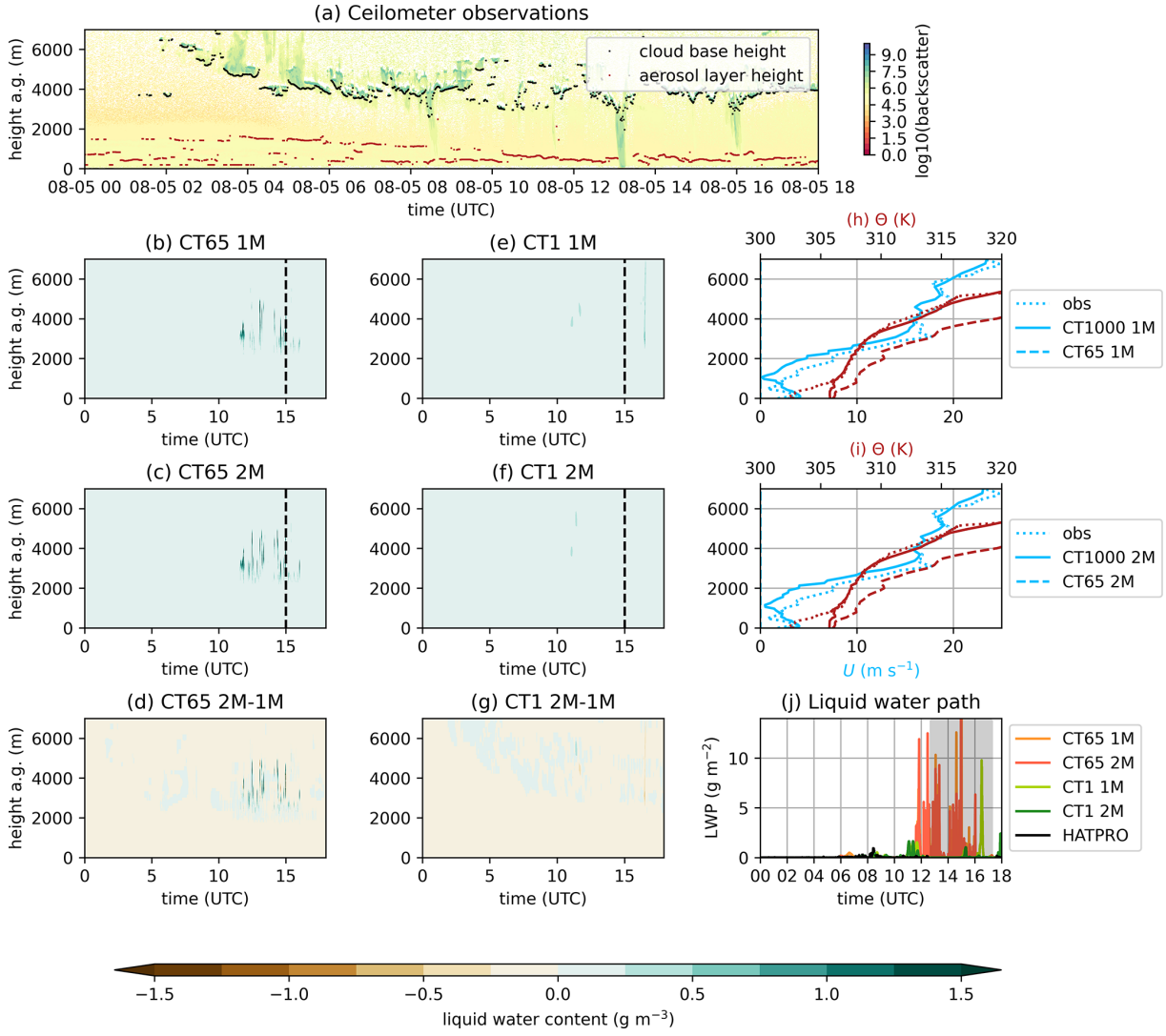

Figure 10. The date of 5 August 2019 at the Inn Valley floor. **(a)** Ceilometer observations showing cloud backscatter (colors), with the cloud base height (black dots) and aerosol layer height (red dots) determined by the instrument. **(b–g)** Time series of model output of liquid water content from simulations CT65 1M **(b, c)** and CT1 1M **(e, f)**, with 1M **(b, e)** and 2M **(c, f)**, respectively. Panels **(d)** and **(g)** show the difference between the 2M and 1M schemes. The color bar is valid for all panels showing LWC. **(h, i)** Vertical profiles along the dashed line in panels **(b)**, **(e)**, **(c)**, and **(f)** of the potential temperature (red) and horizontal wind speed (blue) for radiosonde observations (dots), CT1 (full lines), and CT65 (dashed lines) from 15:00 UTC. **(j)** LWP observations from the HATPRO (black; instrument failure from 12:30–17:00 UTC; shaded grey area) and LWP model output from the respective simulations (colors).

an interruption at around 04:00 UTC. However, the breakup of the stratus layer together with the evolution of the daytime boundary layer is simulated accurately, and in the afternoon, small-scale altocumulus clouds are present as in the observations. As in the CT65 runs, the 2M leads to higher LWC contents (Fig. 12g). The CT1 runs simulate the LWP time series in a realistic way (i.e., LWP maxima the in observations and model are synchronous); however, the absolute values of LWP are underestimated by the model by about 5 g m^{-2}.

In contrast to the other case study in complex terrain (5 August 2019), the model is able to simulate realistic potential temperature and horizontal wind speed profiles in the valley for both resolutions (Fig. 12h and i), and this also leads to fewer discrepancies in cloud formation. Furthermore, since local circulations are well represented (Fig. 13g, k, h, and l), there is no large difference in cloud cover between the two mesh sizes and microphysics schemes (Fig. 11).

3.3 Discussion and comparison of the four cases

In general, the observations from the field campaigns proved to be an excellent data pool for model validation. However, our comparison with observations deviates from classical NWP model validation methods (e.g., forecast skills, calcu-

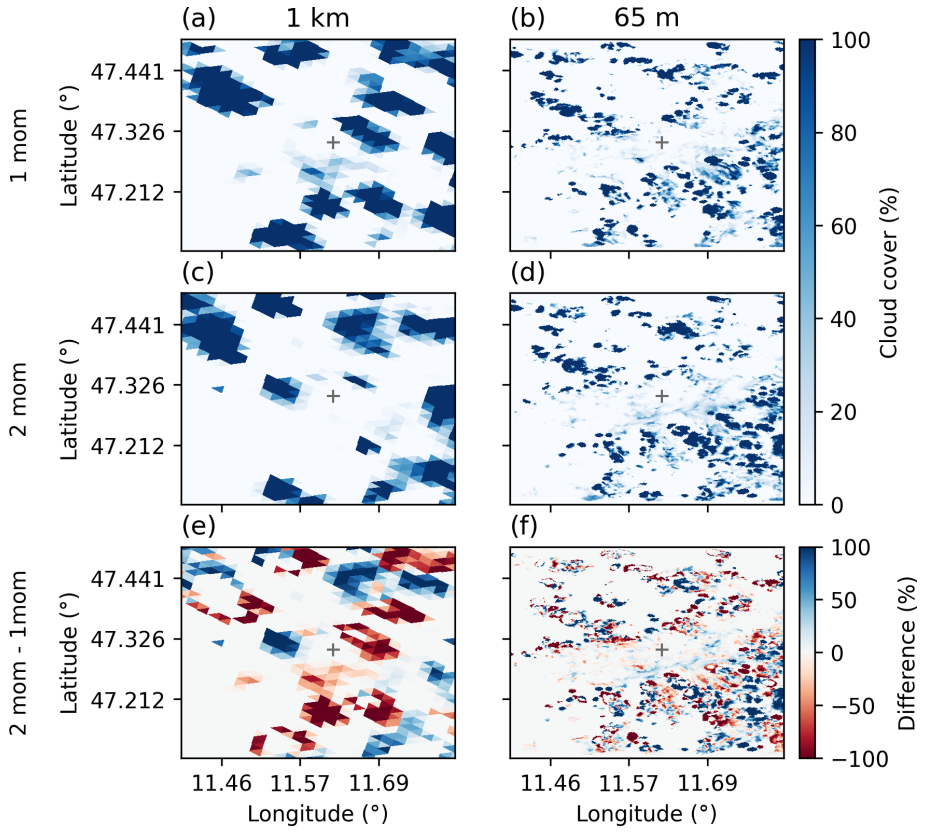

Figure 11. Comparison of cloud cover extent (%) at ∼ 4000 m a.g.l. for the case study on 14 August 2019 at 09:00 UTC (closest time step to the all-sky camera snapshot in Fig. 1h) for CT1 **(a, c, e)** and CT65 **(b, d, f)** in the 1M **(a, b)** and 2M **(c, d)** configurations and their difference (2M–1M, **e, f**). The "+" symbol marks the CROSSINN field site. The domain of HT1 was enlarged to show the same area as HT65.

lating bias, and root mean square error). Therefore, most of our analysis is of qualitative matter, but still we provided an overview of the performance of the microphysics schemes and possible model shortcomings. Furthermore, we have to consider in our analysis that single-point observations are not entirely representative of cloud patterns at a certain location. We tried to overcome this spatial problem by including model output from five output grid points to allow information on the spatial variability as it is represented in the model. Besides the point observations with the remote sensing systems, we provided a qualitative analysis in comparison with all-sky camera images. The detailed comparison with the observations from measurement campaigns allowed us to perform a one-of-a-kind analysis of modeled cloud properties and the related physical processes.

For all four cases, the comparison with microwave radiometer and radiosonde profiles shows a realistic representation of the diurnal temperature cycle (see Figs. B2, B4, and C1), with only small (< 1 °C) differences between the horizontal resolutions, underlying terrain, and microphysics scheme. However, we noticed that the choice of the cloud microphysics scheme can impact the temperature profile in a way that we cannot fully explain. The largest differences in temperatures are notable in the 1 km simulations. For example, for the case study on 20 March 2022, we see cooler temperatures inside the cloud with 2M, while above the cloud, a positive temperature anomaly is notable (Fig. B2). This is contrary to what we would normally expect (i.e., higher temperatures inside the cloud region due to latent heat release and cooler temperatures above the cloud due to cloud-top cooling). This response is not present in the 65 m simulations, where the temperature profiles are more realistic. We hypothesize that the reduced vertical mixing at lower resolutions (see Figs. 4, 8, and 13) leads to an unphysical model response in the 1 km simulations; however, further research is needed to investigate this model behavior.

Regarding the cloud cover, we see that the 65 m simulations achieve a better representation of the investigated cloud types, although there are some shortcomings such as no full-cloud cover for the case of stratocumulus clouds (31 January 2023) or clouds that are too short-lived (in all cases). There are no systematic changes when switching from 1M to 2M. For both horizontal resolutions, both microphysics schemes perform similarly with respect to cloud cover occurrences. Instead, we see random differences between the two schemes, which leads to spatial shifts in the clouds.

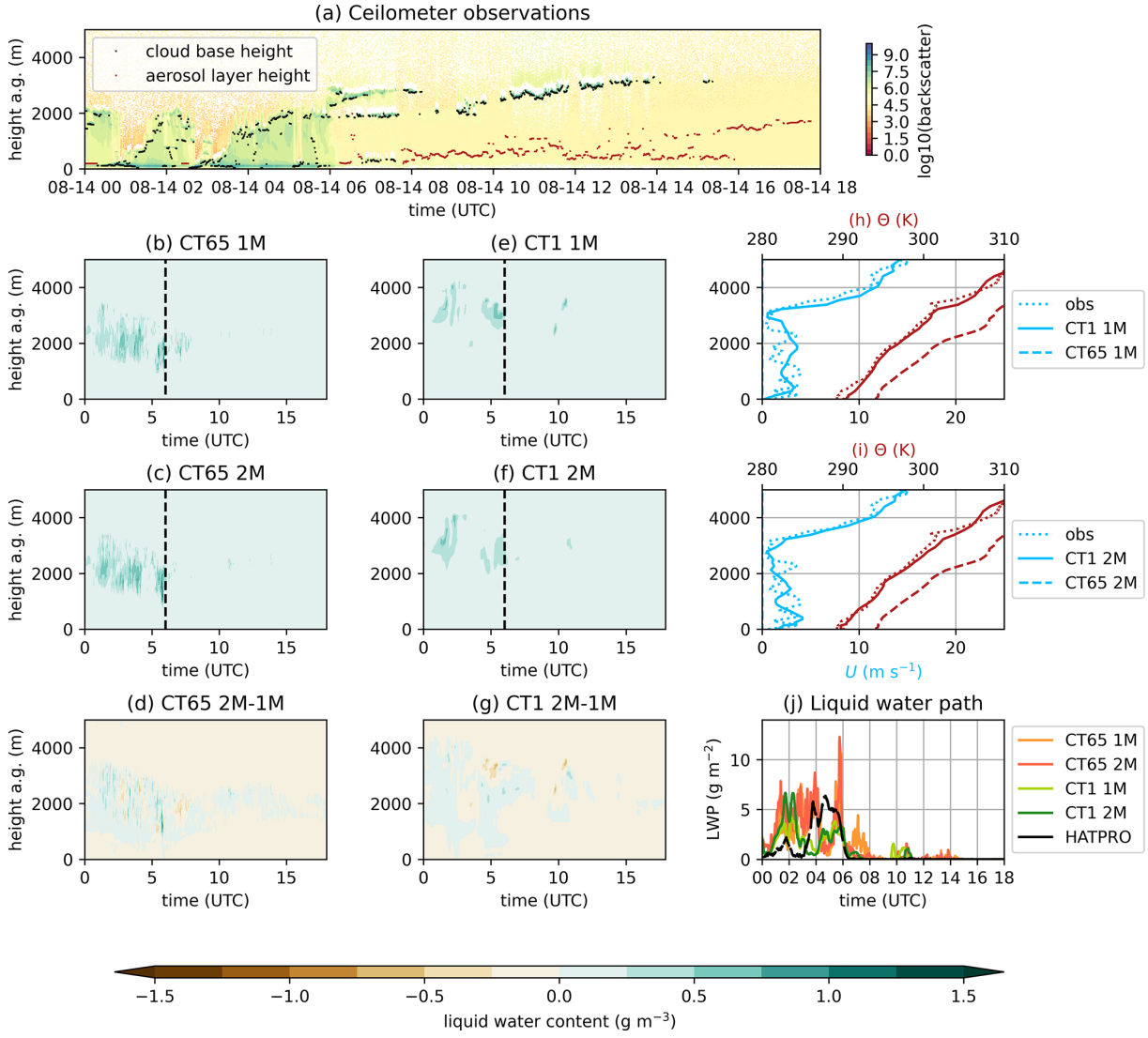

Figure 12. The date of 14 August 2019 at the Inn Valley floor. **(a)** Ceilometer observations showing the cloud backscatter (colors), with the cloud base height (black dots) and the aerosol layer height (red dots) determined by the instrument. **(b–g)** Time series of model output of liquid water content from simulations CT65 1M **(b, c)** and CT1 1M **(e, f)** with 1M **(b, e)** and 2M **(c, f)**, respectively. Panels **(d)** and **(g)** show the difference between the 2M and 1M schemes. The color bar is valid for all panels showing LWC. **(h, i)** Vertical profiles along the dashed line in panels **(b)**, **(e)**, **(c)**, and **(f)** of potential temperature (red) and horizontal wind speed (blue) of radiosonde observations (dots), CT1 (full lines), and CT65 (dashed lines) from 15:00 UTC. **(j)** LWP observations from the HATPRO (black) and LWP model output from the respective simulations (colors).

For the hilly terrain with a focus on wintertime clouds, it is evident that the HT1 simulations predict higher LWCs than the HT65 simulations and the observations. As expected, the IWC for HT1 was close to zero. On the other hand, the HT65 simulations qualitatively agree better with observations regarding IWC and cloud height but fail to simulate any LWC for the cases. This points towards the model struggling to represent mixed-phase clouds, as it either retains too much liquid phase or fully glaciates the clouds. A quantitative analysis showed that LWC and IWC are strongly underestimated in the model compared to the observations with 2M showing higher contents (and paths). The differences between the two horizontal resolutions are summarized in Fig. 14 for all case studies in the form of histograms. It is clear that over hilly terrain the kilometric simulations have more liquid clouds (Fig. 14a, d, j, and m), while the LESs have more IWC and IWP (Fig. 14b, e, k, and n). Moreover, the timing (20 March 2022) and the longevity (31 March 2023) are still challenging for the model to capture fully. For the summer cases in complex terrain, we also see that the cloud formation and cloud features are better represented in the CT65 simulations compared to the CT1 runs. Nevertheless, the dis-

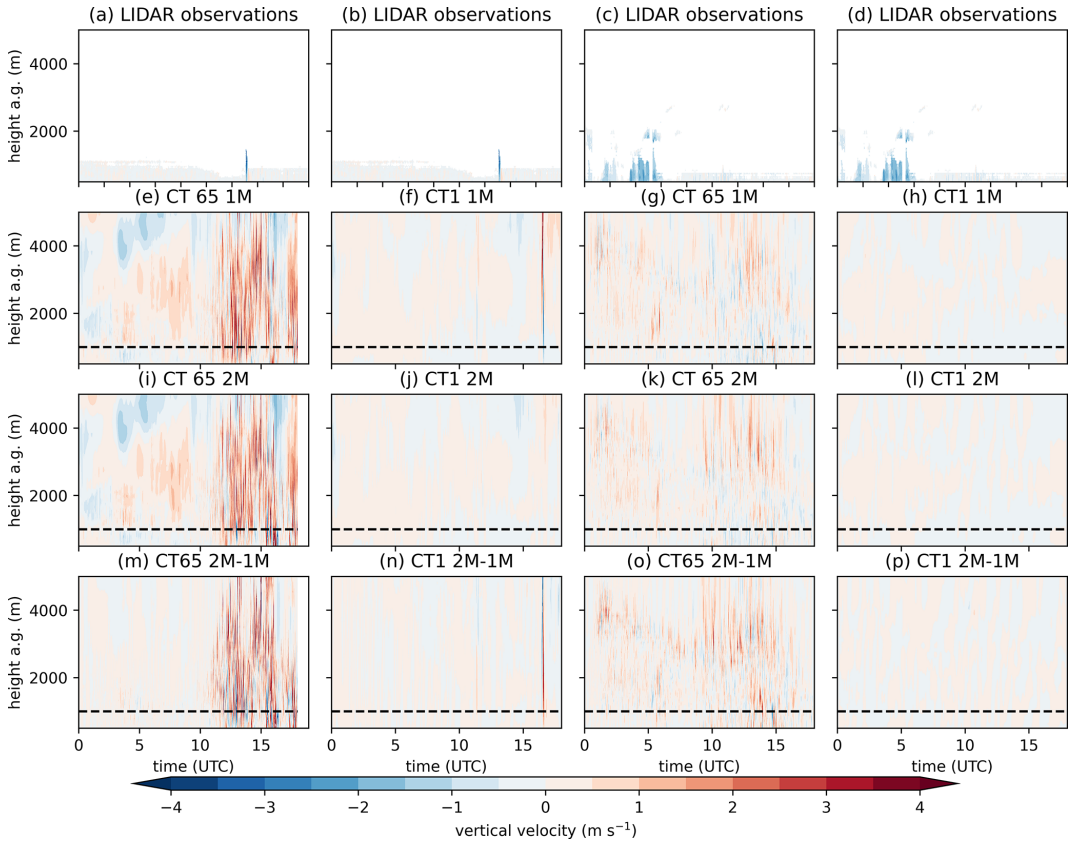

Figure 13. Time evolution of vertical profiles of vertical velocity from the SL88 lidar observations **(a–d)**, model output from the different horizontal resolutions and microphysics schemes **(f–l)**, and their differences **(m–p)** from the two CT case studies at the valley floor, respectively. The dashed lines denotes the average range of lidar observations to put the model output into context.

crepancy with the 1 km simulations is much less than for the hilly terrain, while the largest difference in LWC simulation is visible for the 7 August case study (altocumulus clouds; Fig. 14c and f). Interestingly, the kilometric simulations perform fairly well, especially for the case on 14 August 2019 (Fig. 14l and o). The better agreement between CT1 and CT65 is also noticeable in Fig. 14. Contrary to the hilly terrain simulations, the predicted LWPs for the complex terrain simulations agree reasonably well with the observations. Similar to the hilly terrain simulations, the longevity and timing of the clouds are not easily captured by the model because either it shows a cloud formation that is too late (5 August 2019) or it shows a dissipation of cumulus clouds that is too early (14 August 2019).

One reason for the differences between the two horizontal resolutions is that the sub-hectometric simulations lead to a more realistic representation of vertical velocities. This leads to an earlier onset of cloud formation, given that especially updrafts lead to the supersaturation required for cloud droplet and ice crystal formation. This highlights the current limitations of operational weather forecasts that cannot resolve these small-scale vertical velocities, leading to an unrealistic representation of the cloud cover. We also see that while the 1M is fairly good at capturing the different cloud types, the 2M still outperforms it in terms of cloud microphysical properties (e.g., LWC and IWC). The advantages of 2M was also discussed by Bryan and Morrison (2012) and Kovačević and Ćurić (2015), while Baldauf et al. (2011) and Kondo et al. (2021) found that 1M and 2M behave similarly. We further note that, especially for the investigated wintertime clouds over the hilly terrain, the 2M performs better in representing the cloud characteristics. Over complex terrain, the differences appeared to be less significant. However, we want to highlight that 1M requires prescribed cloud droplet number concentrations, while 2M allows for variable cloud droplet number concentrations based on the updraft velocity. This is a more physical representation of the cloud formation process and should be considered when simulating clouds. Furthermore, for investigating aerosol–cloud interactions, 2M is crucial for coupling the aerosol number concentrations with cloud droplet number concentrations.

4 Conclusions

We conducted numerical simulations with the ICON model at two horizontal grid spacings ($\Delta x = 65$ m and $\Delta x = 1$ km)

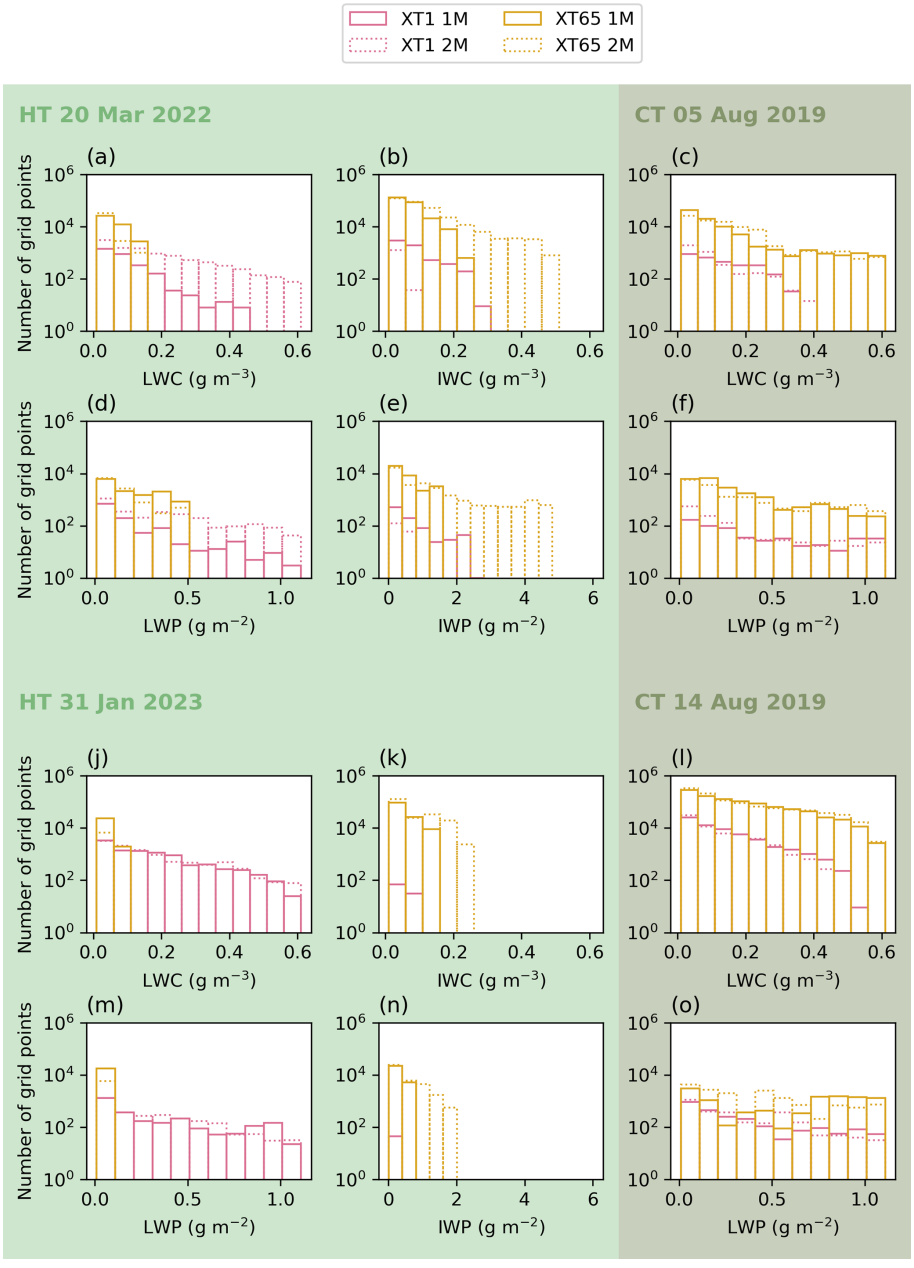

Figure 14. Histograms for LWC ($g\,m^{-3}$; bin width $= 0.05\,g\,m^{-3}$), IWC ($g\,m^{-3}$; bin width $= 0.05\,g\,m^{-3}$), LWP ($g\,m^{-2}$; bin width $= 0.1\,g\,m^{-2}$), and IWP ($g\,m^{-2}$; bin width $= 0.4\,g\,m^{-2}$) for all case studies sorted in hilly terrain (HT; light green) and complex terrain (CT; dark green) simulations. Similar to Tables 3 and 4, a threshold value of $0.01\,g\,m^{-3}$ is applied before computing the histograms. Note the different scales for the x axes.

for four case studies to investigate the impact of terrain, mesh size, and microphysics scheme (one moment vs. two moment) on the formation of two cloud types (altocumulus and stratocumulus clouds) at two locations in Europe (hilly vs. complex terrain). The simulations are validated with observations of LWC, IWC, LWP, and meteorological variables (e.g., temperature and vertical velocity) from two measurement campaigns (CLOUDLAB, hilly terrain, and CROSSINN, complex terrain). The detailed model validation study leads us to the following conclusions:

- The diurnal evolution of temperature is represented at both mesh sizes and locations in a realistic way and in qualitative agreement with observations. However, the $\Delta x = 65$ m simulations clearly outperform the kilometric simulations in terms of vertical velocity representation.

- This realistic representation of up- and downdrafts consequently leads to a better representation of clouds in the $\Delta x = 65$ m simulations in terms of cloud formation, duration, and microphysical properties.
- The cloud microphysical properties are often better represented in simulations with the two-moment scheme than when compared to the one-moment scheme, which may come from the more physical representation of cloud processes such as cloud droplet formation or ice nucleation. This can be seen in the liquid and ice water content but also in the timing of the cloud formation and the height of the clouds.
- When we compare cloud types, we note that the model generally performs better in the representation of convective clouds (cumulus and stratocumulus clouds) than for stratiform clouds (altocumulus clouds). This applies to both regions (hilly and complex terrain).
- The observations from the two independent measurement campaigns (CLOUDLAB and CROSSINN) provided a valuable dataset and were essential for validating the representation of clouds in numerical weather prediction models at high horizontal resolution.

This study provides a first evaluation of mid-level clouds over hilly and complex terrain in the form of case studies in ICON. This can, of course, be expanded to other cloud types and over a larger time period to increase the statistical representation. A future, more in-depth, analysis is needed to include the comparison of the process rates between the two microphysics schemes. Furthermore, no sensitivity analysis was done to perturb the single parameterization within the cloud microphysics schemes, which could be a further step in a more in-depth evaluation. Still, the study serves as a direct comparison of cloud representation at kilometric and sub-hectometric grid spacings with detailed observations of cloud properties and gives a valuable overview on the limitations of kilometric models for representing clouds.

Appendix A: Distribution of model levels

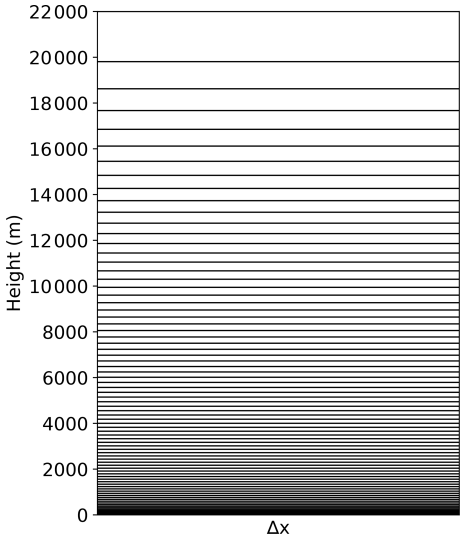

Figure A1. Mean height of the 80 model levels, with the model top at 22 000 m that is valid for all simulations.

Appendix B: Additional figures for HT simulations

B1 20 March 2022: altocumulus clouds

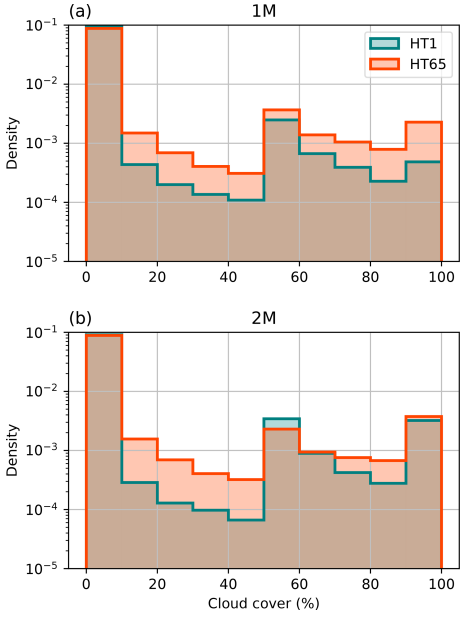

Figure B1. Probability density figures for the cloud cover (%) of HT1 (teal) and HT65 (red) with 1M **(a)** and 2M **(b)** over all 5 min model output time steps and all height levels where the cloud was present. The domain and time period included in this analysis are the same as in Fig. 3. The bin width is set to 10 %.

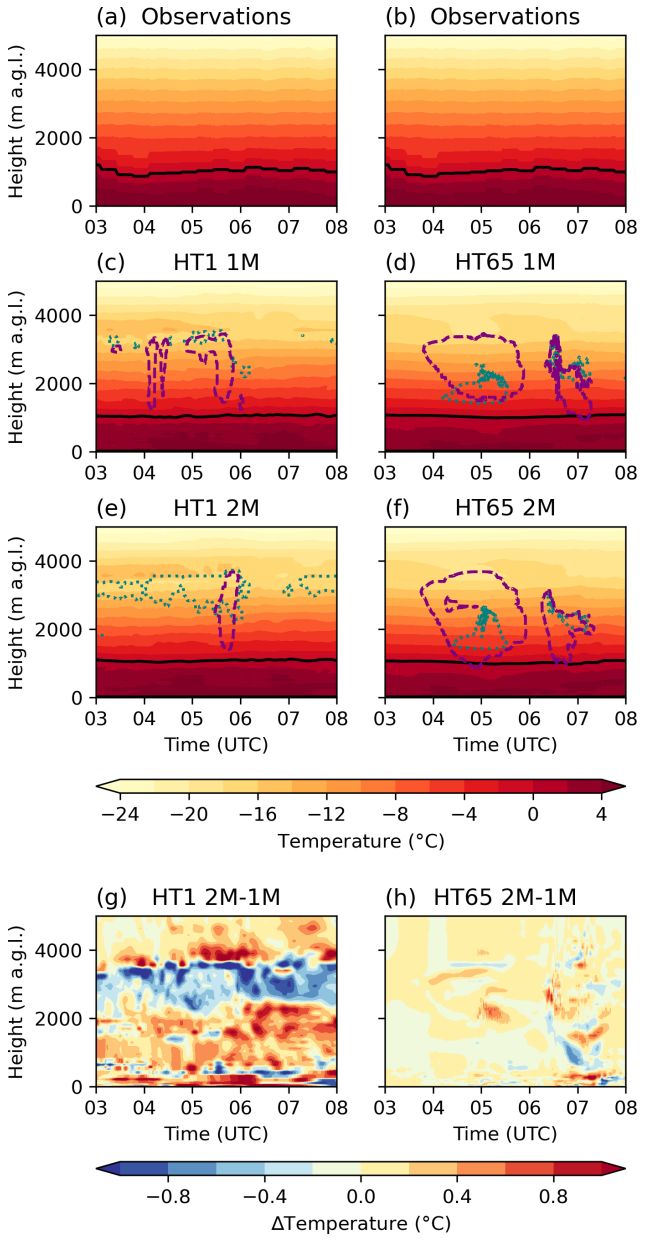

Figure B2. Case study on 20 March 2022. Hovmöller diagrams for temperature (°C) measured by a microwave radiometer **(a, b)** and simulated by the model for both resolutions (HT1 and HT65) and both cloud microphysics schemes (1M and 2M) **(c–f)**. The black line indicates the 0 °C isotherm (black line). The dashed purple line shows the IWC = 0.01 g m^{-3}, while the dotted teal line shows the LWC = 0.01 g m^{-3}. These serve as an indicator for the position of the cloud. The last row **(g, h)** shows the differences between 2M and 1M for each resolution.

B2 31 January 2023: stratocumulus clouds

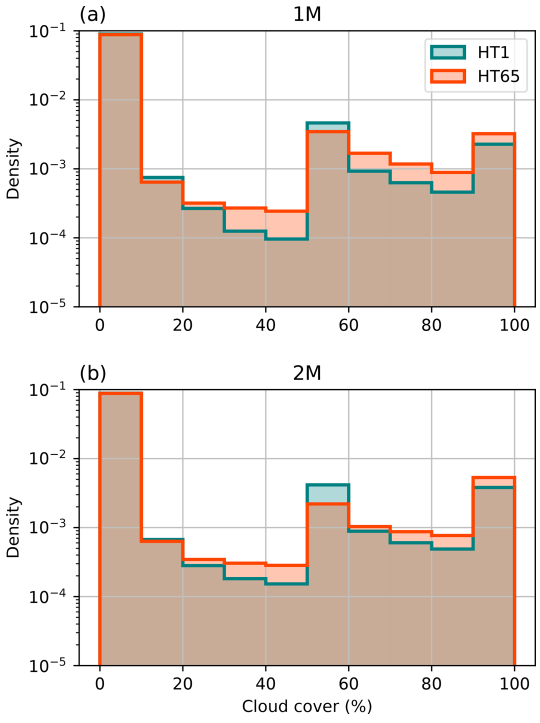

Figure B3. Probability density figures for the cloud cover (%) of HT1 (teal) and HT65 (red) with 1M **(a)** and 2M **(b)** over all 5 min model output time steps and all height levels where the cloud was present. The domain and time period included in this analysis are the same as in Fig. 7. The bin width is set to 10 %.

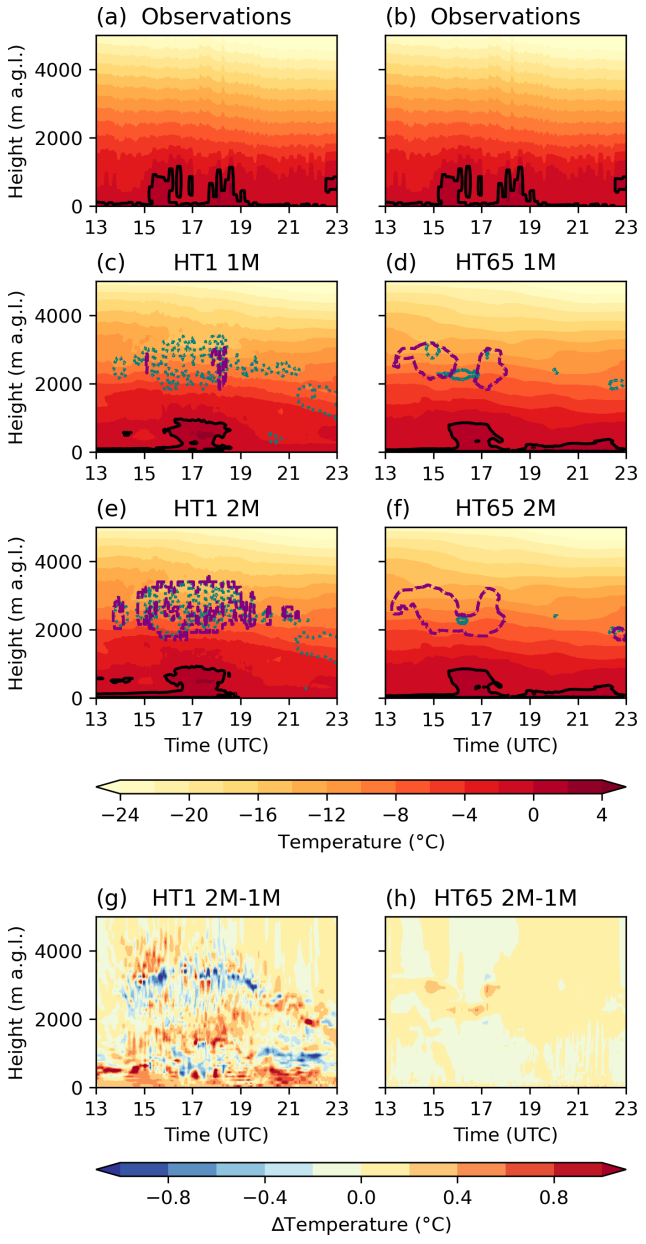

Figure B4. Case study 31 January 2023. Hovmöller diagrams for temperature (°C) measured by a microwave radiometer **(a, b)** and simulated by the model for both resolutions (HT1 and HT65) and both cloud microphysics schemes (1M and 2M) **(c–f)**. The black line indicates the 0 °C isotherm (black line). The dashed purple line shows the IWC = 0.01 g m^{-3}, while the dotted teal line shows the LWC = 0.01 g m^{-3}. These serve as an indicator for the position of the cloud. The last row **(g, h)** shows the differences between 2M and 1M for each resolution.

Appendix C: Additional figures for CT simulations

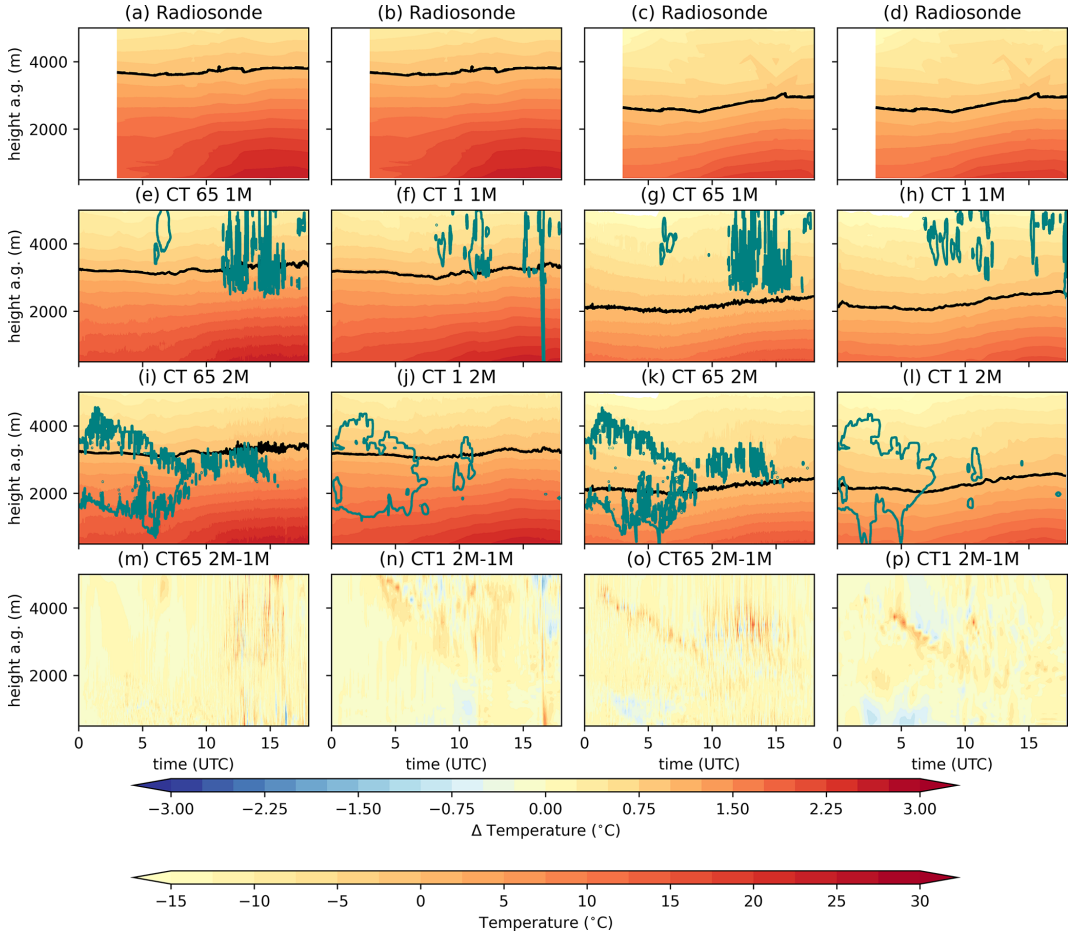

Figure C1. Time evolution of vertical profiles of air temperature from radiosonde observations **(a–d)**, model output from the different horizontal resolutions and microphysics schemes **(f–l)**, and their differences **(m–p)** from the two CT case studies (5 August 2019 (**a, b, e, f, i, j, m, n**) and 14 August 2029 (**c, d, g, h, k, l, o, p**)) at the valley floor, respectively. The black lines denote the 0 °C line, and the green contours show areas where LWC > 0.01 g m^3.

C1 5 August 2019: altocumulus clouds

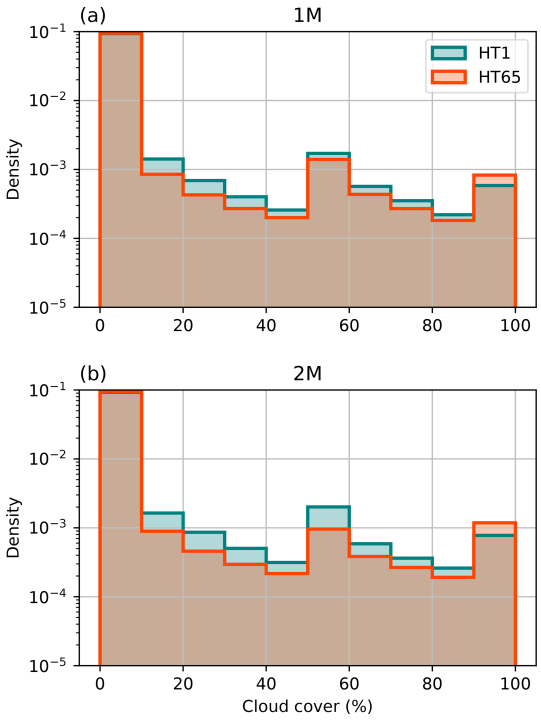

Figure C2. Probability density figures for the cloud cover (%) of HT1 (teal) and HT65 (red) with 1M **(a)** and 2M **(b)** over all 5 min model output time steps and all height levels where the cloud was present. The domain and time period included in this analysis are the same as in Fig. 9. The bin width is set to 10 %.

C2 14 August 2019: altocumulus clouds

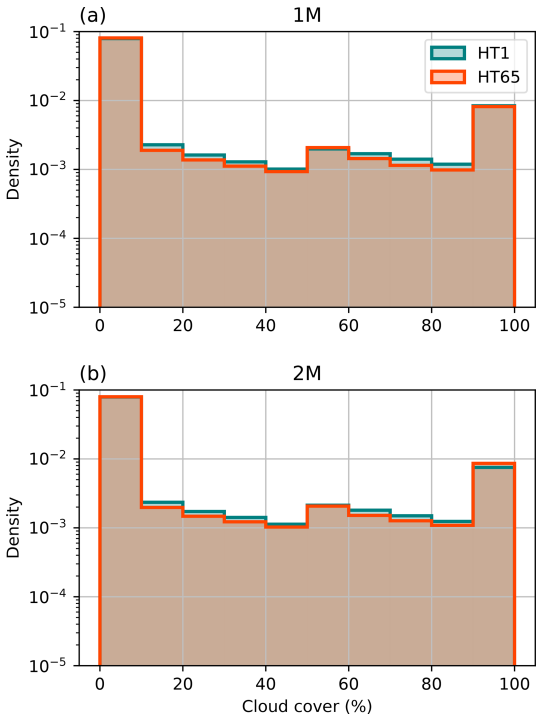

Figure C3. Probability density figures for the cloud cover (%) of HT1 (teal) and HT65 (red) with 1M **(a)** and 2M **(b)** over all 5 min model output time steps and all height levels where the cloud was present. The domain and time period included in this analysis are the same as in Fig. 11. The bin width is set to 10 %.

Appendix D: Hydrometeor number concentrations

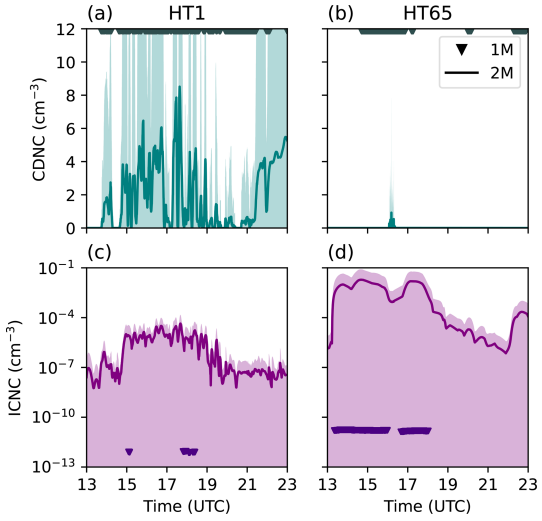

Figure D1. Simulated cloud droplet **(a, b)** and ice crystal **(c, d)** number concentrations (CDNC and ICNC, respectively) for 31 January 2023 for both resolutions (HT1 and HT65; **a/c** and **b/d**, respectively). The number concentrations from 1M are shown as markers whenever there is a cloud present. In 1M, CDNC $= 200\,\mathrm{cm}^{-3}$ (prescribed, markers only for indicating cloudy conditions), while ICNC is calculated as a function of temperature following Cooper (1986) (diagnosed). The predicted quantities from 2M are shown as means (solid lines) $\pm$ standard deviations (shading).

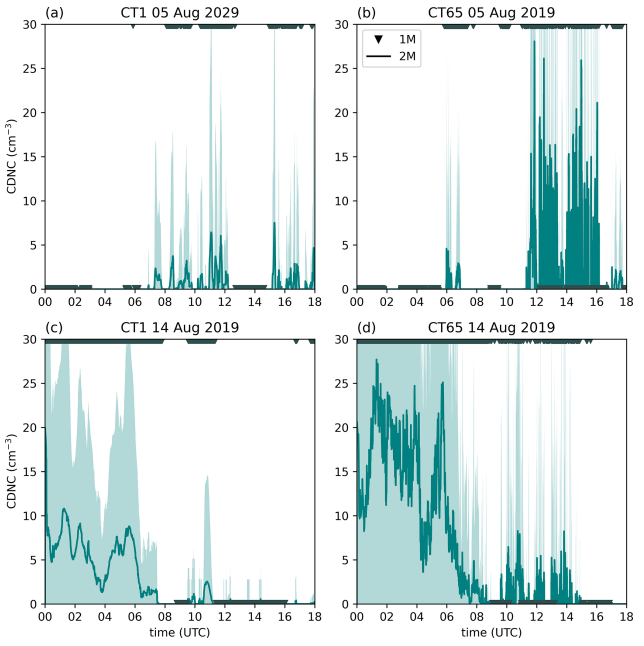

Figure D2. Simulated cloud droplet number concentrations (CDNCs) for 5 August **(a, b)** and 14 August **(c, d)** for both resolutions (CT1 and CT65; **a/c** and **b/d**, respectively). The number concentrations from 1M are shown as markers whenever there is a cloud present. In 1M, CDNC $= 200\,\mathrm{cm}^{-3}$ (prescribed, markers only for indicating cloudy conditions). The predicted quantities from 2M are shown as means (solid lines) $\pm$ standard deviations (shading).

Code and data availability. Observational data from the CROSSINN campaign (Adler et al., 2021b) can be downloaded from Adler et al. (2021a) (https://doi.org/10.5445/IR/1000127577) [radiosondes, all-sky camera, ceilometer, and HATPRO] and Gohm et al. (2021) (https://doi.org/10.5281/zenodo.4585577) [lidar data]. Model and observational data are available from Omanovic et al. (2024c) (https://doi.org/10.5281/zenodo.14045157). Analysis and plotting scripts are available from Omanovic et al. (2024d) (https://doi.org/10.5281/zenodo.14045181). We used the ICON model code version 2.6.6 for our simulations. The open-source model code can be obtained from https://gitlab.dkrz.de/icon/icon-model (DWD et al., 2024).

Video supplement. The video compilations for the all-sky cameras and model cloud cover can be found in Omanovic et al. (2024b) (https://doi.org/10.5281/zenodo.11658150).

Author contributions. NO conceived the study idea. NO and BG designed and conducted the hilly terrain (NO) and complex terrain (BG) simulations, respectively. Both authors wrote the paper and performed model output analysis and observations. UL provided input to the paper writing and results discussion.

Competing interests. The contact author has declared that none of the authors has any competing interests.

Acknowledgements. We thank the two anonymous referees for providing thoughtful comments leading to an improvement in the paper.

Financial support. The CLOUDLAB project (Nadja Omanovic) has received funding from the European Research Council (ERC) under the European Union's Horizon 2020 research and innovation program (grant agreement no. 101021272 CLOUDLAB). This work was supported by a grant from the Swiss National Supercomputing Centre (CSCS) under project ID s1144 (Nadja Omanovic) and d121 (Brigitta Goger). Brigitta Goger has been funded by EXCLAIM, a project by ETH Zurich.

Review statement. This paper was edited by Hailong Wang and reviewed by two anonymous referees.

References

Adler, B., Babić, N., Kalthoff, N., and Wieser, A.: CROSSINN (Cross-valley flow in the Inn Valley investigated by dual-Doppler lidar measurements) – KITcube data sets [CHM 15k, GRAW, HATPRO2, Mobotix, Photos], KIT [data set], https://doi.org/10.5445/IR/1000127577, 2021a.

Adler, B., Gohm, A., Kalthoff, N., Babić, N., Corsmeier, U., Lehner, M., Rotach, M. W., Haid, M., Markmann, P., Gast, E., Tsaknakis, G., and Georgoussis, G.: CROSSINN: A Field Experiment to Study the Three-Dimensional Flow Structure in the Inn Valley, Austria, B. Am. Meteorol. Soc., 102, E38–E60, https://doi.org/10.1175/BAMS-D-19-0283.1, 2021b.

Allen, G., Coe, H., Clarke, A., Bretherton, C., Wood, R, Abel, S. J., Barrett, P., Brown, P., George, R., Freitag, S., McNaughton, C., Howell, S., Shank, L., Kapustin, V., Brekhovskikh, V., Kleinman, L., Lee, Y.-N., Springston, S., Toniazzo, T., Krejci, R., Fochesatto, J., Shaw, G., Krecl, P., Brooks, B., McMeeking, G., Bower, K. N., Williams, P. I., Crosier, J., Crawford, I., Connolly, P., Allan, J. D., Covert, D., Bandy, A. R., Russell, L. M., Trembath, J., Bart, M., McQuaid, J. B., Wang, J., and Chand, D.: South East Pacific atmospheric composition and variability sampled along 20° S during VOCALS-REx, Atmos. Chem. Phys., 11, 5237–5262, https://doi.org/10.5194/acp-11-5237-2011, 2011.

Andrejczuk, M., Reisner, J. M., Henson, B., Dubey, M. K., and Jeffery, C. A.: The potential impacts of pollution on a nondrizzling stratus deck: Does aerosol number matter more than type?, J. Geophys. Res.-Atmos., 113, D19204, https://doi.org/10.1029/2007JD009445, 2008.

Andrejczuk, M., Grabowski, W. W., Reisner, J., and Gadian, A.: Cloud-aerosol interactions for boundary layer stratocumulus in the Lagrangian Cloud Model, J. Geophys. Res.-Atmos., 115, D22214, https://doi.org/10.1029/2010JD014248, 2010.

Atlas, R. L., Bretherton, C. S., Blossey, P. N., Gettelman, A., Bardeen, C., Lin, P., and Ming, Y.: How Well Do Large-Eddy Simulations and Global Climate Models Represent Observed Boundary Layer Structures and Low Clouds Over the Summertime Southern Ocean?, J. Adv. Model. Earth Syst., 12, e2020MS002205, https://doi.org/10.1029/2020MS002205, 2020.

Baldauf, M., Seifert, A., Förstner, J., Majewski, D., Raschendorfer, M., and Reinhardt, T.: Operational Convective-Scale Numerical Weather Prediction with the COSMO Model: Description and Sensitivities, Mon. Weather Rev., 139, 3887–3905, https://doi.org/10.1175/MWR-D-10-05013.1, 2011.

Ban, N., Schmidli, J., and Schär, C.: Evaluation of the convection-resolving regional climate modeling approach in decade-long simulations, J. Geophys. Res.-Atmos., 119, 7889–7907, https://doi.org/10.1002/2014JD021478, 2014.

Bauer, P., Thorpe, A., and Brunet, G.: The quiet revolution of numerical weather prediction, Nature, 525, 47–55, https://doi.org/10.1038/nature14956, 2015.

Bergeron, T.: On the physics of clouds and precipitation, in: Proc. 5th Assembly UGGI, September 1935, Lisbon, Portugal, 15–180, 1935.

Bretherton, C. S. and Blossey, P. N.: Understanding Mesoscale Aggregation of Shallow Cumulus Convection Using Large-Eddy Simulation, J. Adv. Model. Earth Syst., 9, 2798–2821, https://doi.org/10.1002/2017MS000981, 2017.

Bretherton, C. S., Blossey, P. N., and Uchida, J.: Cloud droplet sedimentation, entrainment efficiency, and subtropical stratocumulus albedo, Geophys. Res. Lett., 34, L03813, https://doi.org/10.1029/2006GL027648, 2007.

Bryan, G. H. and Morrison, H.: Sensitivity of a Simulated Squall Line to Horizontal Resolution and Parameterization of Microphysics, Mon. Weather Rev., 140, 202–225, https://doi.org/10.1175/MWR-D-11-00046.1, 2012.

Buzzi, M.: Challenges in Operational Wintertime Weather Prediction at High Resolution in Complex Terrain, PhD thesis, ETH Zurich, https://doi.org/10.3929/ethz-a-005698833, 2008.

Chow, F. K., Schär, C., Ban, N., Lundquist, K. A., Schlemmer, L., and Shi, X.: Crossing Multiple Gray Zones in the Transition from Mesoscale to Microscale Simulation over Complex Terrain, Atmosphere, 10, 274, https://doi.org/10.3390/atmos10050274, 2019.

Cooper, W. A.: Ice Initiation in Natural Clouds, in: Precipitation Enhancement, edited by: Braham, R. R. J., American Meteorological Society Boston, MA, Chicago, Illinois, USA, 29–32, ISBN 978-0-933876-65-1, https://doi.org/10.1007/978-1-935704-17-1, 1986.

Davies, T.: Lateral Boundary Conditions for Limited Area Models, Q. J. Royal Meteorol. Soc., 140, 185–196, https://doi.org/10.1002/qj.2127, 2014.

Delbeke, L., Wang, C., Tulet, P., Denjean, C., Zouzoua, M., Maury, N., and Deroubaix, A.: The impact of aerosols on stratiform clouds over southern West Africa: a large-eddy-

simulation study, Atmos. Chem. Phys, 23, 13329–13354, https://doi.org/10.5194/acp-23-13329-2023, 2023.

DeMott, P. J., Prenni, A. J., McMeeking, G. R., Sullivan, R. C., Petters, M. D., Tobo, Y., Niemand, M., Möhler, O., Snider, J. R., Wang, Z., and Kreidenweis, S. M.: Integrating laboratory and field data to quantify the immersion freezing ice nucleation activity of mineral dust particles, Atmos. Chem. Phys, 15, 393–409, https://doi.org/10.5194/acp-15-393-2015, 2015.

Diamond, M. S., Saide, P. E., Zuidema, P., Ackerman, A. S., Doherty, S. J., Fridlind, A. M., Gordon, H., Howes, C., Kazil, J., Yamaguchi, T., Zhang, J., Feingold, G., and Wood, R.: Cloud adjustments from large-scale smoke-circulation interactions strongly modulate the southeastern Atlantic stratocumulus-to-cumulus transition, Atmos. Chem. Phys, 22, 12113–12151, https://doi.org/10.5194/acp-22-12113-2022, 2022.

Dipankar, A., Stevens, B., Heinze, R., Moseley, C., Zängl, G., Giorgetta, M., and Brdar, S.: Large Eddy Simulation Using the General Circulation Model ICON, J. Adv. Model. Earth Syst., 7, 963–986, https://doi.org/10.1002/2015MS000431, 2015.

Doms, G., Förstner, J., Heise, E., Herzog, H.-J., Mironov, D., Raschendorfer, M., Reinhardt, T., Ritter, B., Schrodin, R., Schulz, J.-P., and Vogel, G.: A Description of the Nonhydrostatic Regional COSMO-Model Part II: Physical Parameterizations, COSMO Model, DWD, 41–87, https://doi.org/10.5676/DWD_pub/nwv/cosmo-doc_6.00_II, 2021.

Duynkerke, P. G., de Roode, S. R., van Zanten, M. C., Calvo, J., Cuxart, J., Cheinet, S., Chlond, A., Grenier, H., Jonker, P. J., Köhler, M., Lenderink, G., Lewellen, D., Lappen, C. L., Lock, A. P., Moeng, C. H., Muller, F., Olmeda, D., Piriou, J. M., Sánchez, E., and Sednev, I.: Observations and numerical simulations of the diurnal cycle of the EUROCS stratocumulus case, Q. J. Roy. Meteorol. Soc., 130, 3269–3296, https://doi.org/10.1256/qj.03.139, 2004.

DWD, MPI, DKRZ, KIT, and C2SM: ICON Open Source Release, Gitlab [code], https://gitlab.dkrz.de/icon/icon-model (last access: 13 August 2024), 20024.

Endo, S., Fridlind, A. M., Lin, W., Vogelmann, A. M., Toto, T., Ackerman, A. S., McFarquhar, G. M., Jackson, R. C., Jonsson, H. H., and Liu, Y.: RACORO Continental Boundary Layer Cloud Investigations: 2. Large-eddy Simulations of Cumulus Clouds and Evaluation with in Situ and Ground-Based Observations, J. Geophys. Res.-Atmos., 120, 5993–6014, https://doi.org/10.1002/2014JD022525, 2015.

European Environmental Agency: Copernicus Land Service – Pan-European Component: CORINE Land Cover, http://land.copernicus.eu/pan-european/corine-land-cover/clc-2012 (last access: 3 April 2024), 2017.

FAO/IIASA/ISSCAS/JRC: Harmonized World Soil Database (version 1.2), FAO, Rome, Italy and IIASA, Laxenburg, Austria, http://webarchive.iiasa.ac.at/Research/LUC/External-World-soil-database/HTML/ (last access: 3 April 2024), 2012.

Feingold, G., Walko, R., Stevens, B., and Cotton, W.: Simulations of marine stratocumulus using a new microphysical parameterization scheme, Atmos. Res., 47–48, 505–528, https://doi.org/10.1016/S0169-8095(98)00058-1, 1998.

Findeisen, W.: Kolloid-meteorologische Vorgänge bei der Niederschlagsbildung, Meteorol. Z., 55, 121–133, 1938.

Gerber, F., Besic, N., Sharma, V., Mott, R., Daniels, M., Gabella, M., Berne, A., Germann, U., and Lehning, M.: Spatial variability in snow precipitation and accumulation in COSMO–WRF simulations and radar estimations over complex terrain, The Cryosphere, 12, 3137–3160, https://doi.org/10.5194/tc-12-3137-2018, 2018.

Goger, B. and Dipankar, A.: The impact of mesh size, turbulence parameterization, and land-surface-exchange scheme on simulations of the mountain boundary layer in the hectometric range, Q. J. Roy. Meteorol. Soc., 150, 3853–3873, https://doi.org/10.1002/qj.4799, 2024.

Goger, B., Rotach, M. W., Gohm, A., Fuhrer, O., Stiperski, I., and Holtslag, A. A. M.: The Impact of Three-Dimensional Effects on the Simulation of Turbulence Kinetic Energy in a Major Alpine Valley, Bound.-Lay. Meteorol., 168, 1–27, https://doi.org/10.1007/s10546-018-0341-y, 2018.

Goger, B., Rotach, M. W., Gohm, A., Stiperski, I., Fuhrer, O., and de Morsier, G.: A New Horizontal Length Scale for a Three-Dimensional Turbulence Parameterization in Mesoscale Atmospheric Modeling over Highly Complex Terrain, J. Appl. Meteorol. Clim., 58, 2087–2102, https://doi.org/10.1175/JAMC-D-18-0328.1, 2019.

Goger, B., Stiperski, I., Nicholson, L., and Sauter, T.: Large-eddy simulations of the atmospheric boundary layer over an Alpine glacier: Impact of synoptic flow direction and governing processes, Q. J. Roy. Meteorol. Soc., 148, 1319–1343, https://doi.org/10.1002/qj.4263, 2022.

Gohm, A., Haid, M., and Rotach, M. W.: CROSSINN (Cross-valley flow in the Inn Valley investigated by dual-Doppler lidar measurements) – ACINN Doppler wind lidar data sets (SL88, SLXR142), Zenodo [data set], https://doi.org/10.5281/zenodo.4585577, 2021.

Grabowski, W. W.: Comparison of Eulerian Bin and Lagrangian Particle-Based Microphysics in Simulations of Nonprecipitating Cumulus, J. Atmos. Sci., 77, 3951–3970, https://doi.org/10.1175/JAS-D-20-0100.1, 2020.

Hande, L. B., Engler, C., Hoose, C., and Tegen, I.: Seasonal variability of Saharan desert dust and ice nucleating particles over Europe, Atmos. Chem. Phys., 15, 4389–4397, https://doi.org/10.5194/acp-15-4389-2015, 2015.

Heim, C., Panosetti, D., Schlemmer, L., Leuenberger, D., and Schär, C.: The Influence of the Resolution of Orography on the Simulation of Orographic Moist Convection, Mon. Weather Rev., 148, 2391–2410, https://doi.org/10.1175/MWR-D-19-0247.1, 2020.

Heinze, R., Dipankar, A., Carbajal Henken, C., Moseley, C., Sourdeval, O., Trömel, S., Xie, X., Adamidis, P., Ament, F., Baars, H., Barthlott, C., Behrendt, A., Blahak, U., Bley, S., Brdar, S., Brueck, M., Crewell, S., Deneke, H., Di Girolamo, P., Evaristo, R., Fischer, J., Frank, C., Friederichs, P., Göcke, T., Gorges, K., Hande, L., Hanke, M., Hansen, A., Hege, H.-C., Hoose, C., Jahns, T., Kalthoff, N., Klocke, D., Kneifel, S., Knippertz, P., Kuhn, A., van Laar, T., Macke, A., Maurer, V., Mayer, B., Meyer, C. I., Muppa, S. K., Neggers, R. A. J., Orlandi, E., Pantillon, F., Pospichal, B., Röber, N., Scheck, L., Seifert, A., Seifert, P., Senf, F., Siligam, P., Simmer, C., Steinke, S., Stevens, B., Wapler, K., Weniger, M., Wulfmeyer, V., Zängl, G., Zhang, D., and Quaas, J.: Large-eddy simulations over Germany using ICON: A comprehensive evaluation, Q. J. Roy. Meteorol. Soc., 143, 69–100, https://doi.org/10.1002/qj.2947, 2017a.

Heinze, R., Moseley, C., Böske, L. N., Muppa, S. K., Maurer, V., Raasch, S., and Stevens, B.: Evaluation of large-eddy simulations forced with mesoscale model output for a multi-week period during a measurement campaign, Atmos. Chem. Phys., 17, 7083–7109, https://doi.org/10.5194/acp-17-7083-2017, 2017b.

Henneberger, J., Ramelli, F., Spirig, R., Omanovic, N., Miller, A. J., Fuchs, C., Zhang, H., Bühl, J., Hervo, M., Kanji, Z. A., Ohneiser, K., Radenz, M., Rösch, M., Seifert, P., and Lohmann, U.: Seeding of Supercooled Low Stratus Clouds with a UAV to Study Microphysical Ice Processes – An Introduction to the CLOUDLAB Project, B. Am. Meteorol. Soc., 104, E1962–E1979, https://doi.org/10.1175/BAMS-D-22-0178.1, 2023.

Hentgen, L., Ban, N., Kröner, N., Leutwyler, D., and Schär, C.: Clouds in Convection-Resolving Climate Simulations Over Europe, J. Geophys. Res.-Atmos., 124, 3849–3870, https://doi.org/10.1029/2018JD030150, 2019.

Hersbach, H., Bell, B., Berrisford, P., Hirahara, S., Horányi, A., Muñoz-Sabater, J., Nicolas, J., Peubey, C., Radu, R., Schepers, D., Simmons, A., Soci, C., Abdalla, S., Abellan, X., Balsamo, G., Bechtold, P., Biavati, G., Bidlot, J., Bonavita, M., De Chiara, G., Dahlgren, P., Dee, D., Diamantakis, M., Dragani, R., Flemming, J., Forbes, R., Fuentes, M., Geer, A., Haimberger, L., Healy, S., Hogan, R. J., Hólm, E., Janisková, M., Keeley, S., Laloyaux, P., Lopez, P., Lupu, C., Radnoti, G., de Rosnay, P., Rozum, I., Vamborg, F., Villaume, S., and Thépaut, J.-N.: The ERA5 global reanalysis, Q. J. Roy. Meteorol. Soc., 146, 1999–2049, https://doi.org/10.1002/qj.3803, 2020.

Hoffmann, F.: The Effect of Spurious Cloud Edge Supersaturations in Lagrangian Cloud Models: An Analytical and Numerical Study, Mon. Weather Rev., 144, 107–118, https://doi.org/10.1175/MWR-D-15-0234.1, 2016.

Hogan, R. J. and Bozzo, A.: A Flexible and Efficient Radiation Scheme for the ECMWF Model, J. Adv. Model, Earth Syst., 10, 1990–2008, https://doi.org/10.1029/2018MS001364, 2018.

Hohenegger, C., Korn, P., Linardakis, L., Redler, R., Schnur, R., Adamidis, P., Bao, J., Bastin, S., Behravesh, M., Bergemann, M., Biercamp, J., Bockelmann, H., Brokopf, R., Brüggemann, N., Casaroli, L., Chegini, F., Datseris, G., Esch, M., George, G., Giorgetta, M., Gutjahr, O., Haak, H., Hanke, M., Ilyina, T., Jahns, T., Jungclaus, J., Kern, M., Klocke, D., Kluft, L., Kölling, T., Kornblueh, L., Kosukhin, S., Kroll, C., Lee, J., Mauritsen, T., Mehlmann, C., Mieslinger, T., Naumann, A. K., Paccini, L., Peinado, A., Praturi, D. S., Putrasahan, D., Rast, S., Riddick, T., Roeber, N., Schmidt, H., Schulzweida, U., Schütte, F., Segura, H., Shevchenko, R., Singh, V., Specht, M., Stephan, C. C., von Storch, J.-S., Vogel, R., Wengel, C., Winkler, M., Ziemen, F., Marotzke, J., and Stevens, B.: ICON-Sapphire: simulating the components of the Earth system and their interactions at kilometer and subkilometer scales, Geosci. Model Dev., 16, 779–811, https://doi.org/10.5194/gmd-16-779-2023, 2023.

Howes, C., Saide, P. E., Coe, H., Dobracki, A., Freitag, S., Haywood, J. M., Howell, S. G., Gupta, S., Uin, J., Kacarab, M., Kuang, C., Leung, L. R., Nenes, A., McFarquhar, G. M., Podolske, J., Redemann, J., Sedlacek, A. J., Thornhill, K. L., Wong, J. P. S., Wood, R., Wu, H., Zhang, Y., Zhang, J., and Zuidema, P.: Biomass-burning smoke's properties and its interactions with marine stratocumulus clouds in WRF-CAM5 and southeastern Atlantic field campaigns, Atmos. Chem. Phys., 23, 13911–13940, https://doi.org/10.5194/acp-23-13911-2023, 2023.

Huang, Y., Dong, X., Kay, J. E., Xi, B., and McIlhattan, E. A.: The Climate Response to Increased Cloud Liquid Water over the Arctic in CESM1: A Sensitivity Study of Wegener–Bergeron–Findeisen Process, Clim. Dynam., 56, 3373–3394, https://doi.org/10.1007/s00382-021-05648-5, 2021.

Illingworth, A. J., Hogan, R. J., O'Connor, E. J., Bouniol, D., Brooks, M. E., Delanoé, J., Donovan, D. P., Eastment, J. D., Gaussiat, N., Goddard, J. W. F., Haeffelin, M., Baltink, H. K., Krasnov, O. A., Pelon, J., Piriou, J.-M., Protat, A., Russchenberg, H. W. J., Seifert, A., Tompkins, A. M., van Zadelhoff, G.-J., Vinit, F., Willén, U., Wilson, D. R., and Wrench, C. L.: Cloudnet: Continuous Evaluation of Cloud Profiles in Seven Operational Models Using Ground-Based Observations, B. Am. Meteorol. Soc., 88, 883–898, https://doi.org/10.1175/BAMS-88-6-883, 2007.

Jeong, J.-H., Witte, M. K., and Smalley, M.: Effects of Wind Shear and Aerosol Conditions on the Organization of Precipitating Marine Stratocumulus Clouds, Q. J. Roy. Meteorol. Soc., 128, e2023JD039081, https://doi.org/10.1029/2023JD039081, 2023.

Jiang, H., Feingold, G., and Cotton, W.: Simulations of aerosol-cloud-dynamical feedbacks resulting from entrainment of aerosol into the marine boundary layer during the Atlantic Stratocumulus Transition Experiment, J. Geophys. Res.-Atmos., 107, 4813, https://doi.org/10.1029/2001JD001502, 2002.

Kanji, Z. A., Ladino, L. A., Wex, H., Boose, Y., Burkert-Kohn, M., Cziczo, D. J., and Krämer, M.: Overview of Ice Nucleating Particles, Meteorol. Monogr., 58, 1.1–1.33, https://doi.org/10.1175/AMSMONOGRAPHS-D-16-0006.1, 2017.

Kay, J. E., Wall, C., Yettella, V., Medeiros, B., Hannay, C., Caldwell, P., and Bitz, C.: Global Climate Impacts of Fixing the Southern Ocean Shortwave Radiation Bias in the Community Earth System Model (CESM), J. Climate, 29, 4617–4636, https://doi.org/10.1175/JCLI-D-15-0358.1, 2016.

Khain, A., Rosenfeld, D., Pokrovsky, A., Blahak, U., and Ryzhkov, A.: The role of CCN in precipitation and hail in a mid-latitude storm as seen in simulations using a spectral (bin) microphysics model in a 2D dynamic frame, Atmos. Res., 99, 129–146, https://doi.org/10.1016/j.atmosres.2010.09.015, 2011.

Klaus, D., Dethloff, K., Dorn, W., Rinke, A., and Wu, D. L.: New Insight of Arctic Cloud Parameterization from Regional Climate Model Simulations, Satellite-Based, and Drifting Station Data, Geophys. Res. Lett., 43, 5450–5459, https://doi.org/10.1002/2015GL067530, 2016.

Kondo, M., Sato, Y., Inatsu, M., and Katsuyama, Y.: Evaluation of Cloud Microphysical Schemes for Winter Snowfall Events in Hokkaido: A Case Study of Snowfall by Winter Monsoon, SOLA, 17, 74–80, https://doi.org/10.2151/sola.2021-012, 2021.

Korolev, A.: Limitations of the Wegener–Bergeron–Findeisen Mechanism in the Evolution of Mixed-Phase Clouds, J. Atmos. Sci., 64, 3372–3375, https://doi.org/10.1175/JAS4035.1, 2007.

Korolev, A. V. and Mazin, I. P.: Supersaturation of Water Vapor in Clouds, J. Atmos. Sci., 60, 2957–2974, https://doi.org/10.1175/1520-0469(2003)060<2957:SOWVIC>2.0.CO;2, 2003.

Kovačević, N. and Ćurić, M.: Precipitation Sensitivity to the Mean Radius of Drop Spectra: Comparison of Single- and Double-

Moment Bulk Microphysical Schemes, Atmosphere, 6, 451–473, https://doi.org/10.3390/atmos6040451, 2015.

Kretzschmar, J., Salzmann, M., Mülmenstädt, J., and Quaas, J.: Arctic Clouds in ECHAM6 and Their Sensitivity to Cloud Microphysics and Surface Fluxes, Atmos. Chem. Phys, 19, 10571–10589, https://doi.org/10.5194/acp-19-10571-2019, 2019.

Lehner, M., Rotach, M. W., and Obleitner, F.: A Method to Identify Synoptically Undisturbed, Clear-Sky Conditions for Valley-Wind Analysis, Bound.-Lay. Meteorol., 173, 435–450, https://doi.org/10.1007/s10546-019-00471-2, 2019.

Leutwyler, D., Fuhrer, O., Lapillonne, X., Lüthi, D., and Schär, C.: Towards European-scale convection-resolving climate simulations with GPUs: a study with COSMO 4.19, Geosci. Model Dev., 9, 3393–3412, https://doi.org/10.5194/gmd-9-3393-2016, 2016.

Li, X.-Y., Wang, H., Christensen, M. W., Chen, J., Tang, S., Kirschler, S., Crosbie, E., Ziemba, L. D., Painemal, D., Corral, A. F., Mccauley, K. A., Dmitrovic, S., Sorooshian, A., Fenn, M., Schlosser, J. S., Stamnes, S., Hair, J. W., Cairns, B., Moore, R., Ferrare, R. A., Shook, M. A., Choi, Y., Diskin, G. S., Digangi, J., Nowak, J. B., Robinson, C., Shingler, T. J., Lee Thornhill, K., and Voigt, C.: Process Modeling of Aerosol-Cloud Interaction in Summertime Precipitating Shallow Cumulus Over the Western North Atlantic, J. Geophys. Res.-Atmos., 129, e2023JD039489, https://doi.org/10.1029/2023JD039489, 2024.

Lilly, D. K.: On the numerical simulation of buoyant convection, Tellus, 14, 148–172, https://doi.org/10.1111/j.2153-3490.1962.tb00128.x, 1962.

Liu, X., Xie, S., Boyle, J., Klein, S. A., Shi, X., Wang, Z., Lin, W., Ghan, S. J., Earle, M., Liu, P. S. K., and Zelenyuk, A.: Testing Cloud Microphysics Parameterizations in NCAR CAM5 with ISDAC and M-PACE Observations, J. Geophys. Res.-Atmos., 116, D00T11, https://doi.org/10.1029/2011JD015889, 2011.

Lohmann, U., Lüönd, F., and Mahrt, F.: An Introduction to Clouds: From the Microscale to Climate, in: 1st Edn., Cambridge University Press, https://doi.org/10.1017/CBO9781139087513, 2016.

Louis, J.-F.: A parametric model of vertical eddy fluxes in the atmosphere, Bound.-Lay. Meteorol., 17, 187–202, https://doi.org/10.1007/BF00117978, 1979.

McIlhattan, E. A., L'Ecuyer, T. S., and Miller, N. B.: Observational Evidence Linking Arctic Supercooled Liquid Cloud Biases in CESM to Snowfall Processes, J. Climate, 30, 4477–4495, https://doi.org/10.1175/JCLI-D-16-0666.1, 2017.

Mellado, J. P., Bretherton, C. S., Stevens, B., and Wyant, M. C.: DNS and LES for Simulating Stratocumulus: Better Together, J. Adv. Model. Earth Syst., 10, 1421–1438, https://doi.org/10.1029/2018MS001312, 2018.

Mikkola, J., Sinclair, V. A., Bister, M., and Bianchi, F.: Daytime along-valley winds in the Himalayas as simulated by the Weather Research and Forecasting (WRF) model, Atmos. Chem. Phys., 23, 821–842, https://doi.org/10.5194/acp-23-821-2023, 2023.

Miller, A. J., Ramelli, F., Fuchs, C., Omanovic, N., Spirig, R., Zhang, H., Lohmann, U., Kanji, Z. A., and Henneberger, J.: Two new multirotor uncrewed aerial vehicles (UAVs) for glaciogenic cloud seeding and aerosol measurements within the CLOUDLAB project, Atmos. Meas. Tech., 17, 601–625, https://doi.org/10.5194/amt-17-601-2024, 2024.

Miyamoto, Y., Kajikawa, Y., Yoshida, R., Yamaura, T., Yashiro, H., and Tomita, H.: Deep moist atmospheric convection in a subkilometer global simulation, Geophys. Res. Lett., 40, 4922–4926, https://doi.org/10.1002/grl.50944, 2013.

Moseley, C., Pscheidt, I., Cioni, G., and Heinze, R.: Impact of resolution on large-eddy simulation of midlatitude summertime convection, Atmos. Chem. Phys., 20, 2891–2910, https://doi.org/10.5194/acp-20-2891-2020, 2020.

Nam, C., Bony, S., Dufresne, J.-L., and Chepfer, H.: The 'too few, too bright' tropical low-cloud problem in CMIP5 models, Geophys. Res. Lett., 39, L21801, https://doi.org/10.1029/2012GL053421, 2012.

NASA/METI/AIST/Japan Spacesystems and US/Japan ASTER Science Team: ASTER Global Digital Elevation Model, NASA EOSDIS Land Processes DAAC, https://doi.org/10.5067/ASTER/ASTGTM.002, 2009.

Omanovic, N., Ferrachat, S., Fuchs, C., Henneberger, J., Miller, A. J., Ohneiser, K., Ramelli, F., Seifert, P., Spirig, R., Zhang, H., and Lohmann, U.: Evaluating the Wegener–Bergeron–Findeisen process in ICON in large-eddy mode with in situ observations from the CLOUDLAB project, Atmos. Chem. Phys., 24, 6825–6844, https://doi.org/10.5194/acp-24-6825-2024, 2024a.

Omanovic, N., Goger, B., and Lohmann, U.: Video supplement for publication "The impact of mesh size and microphysics scheme on the representation of mid-level clouds in the ICON model in hilly and complex terrain", Zenodo [video supplement], https://doi.org/10.5281/zenodo.11658150, 2024b.

Omanovic, N., Goger, B., and Lohmann, U.: Data for publication "The impact of mesh size and microphysics scheme on the representation of mid- level clouds in the ICON model in hilly and complex terrain", Zenodo [data set], https://doi.org/10.5281/zenodo.14045157, 2024c.

Omanovic, N., Goger, B., and Lohmann, U.: Scripts for publication "The impact of mesh size and microphysics scheme on the representation of mid-level clouds in the ICON model in hilly and complex terrain", Zendodo [code], https://doi.org/10.5281/zenodo.14045181, 2024d.

Palmer, T.: The primacy of doubt: Evolution of numerical weather prediction from determinism to probability, J. Adv. Model. Earth Syst., 9, 730–734, https://doi.org/10.1002/2017MS000999, 2017.

Panosetti, D., Böing, S., Schlemmer, L., and Schmidli, J.: Idealized Large-Eddy and Convection-Resolving Simulations of Moist Convection over Mountainous Terrain, J. Atmos. Sci., 73, 4021–4041, https://doi.org/10.1175/JAS-D-15-0341.1, 2016.

Perez, A. B., Diamond, M. S., Bender, F. A. M., Devasthale, A., Schwarz, M., Savre, J., Tonttila, J., Kokkola, H., Lee, H., Painemal, D., and Ekman, A. M. L.: Comparing the simulated influence of biomass burning plumes on low-level clouds over the southeastern Atlantic under varying smoke conditions, Atmos. Chem. Phys, 24, 4591–4610, https://doi.org/10.5194/acp-24-4591-2024, 2024.

Phillips, V. T. J., DeMott, P. J., and Andronache, C.: An Empirical Parameterization of Heterogeneous Ice Nucleation for Multiple Chemical Species of Aerosol, J. Atmos. Sci., 65, 2757–2783, https://doi.org/10.1175/2007JAS2546.1, 2008.

Pressel, K. G., Mishra, S., Schneider, T., Kaul, C. M., and Tan, Z.: Numerics and subgrid-scale modeling in large eddy simulations of stratocumulus clouds, J. Adv. Model. Earth Syst., 9, 1342–1365, https://doi.org/10.1002/2016MS000778, 2017.

Pruppacher, H. R. and Klett, J. D.: Microphysics of Clouds and Precipitation, in: 1st Edn., Springer, Dordrecht, https://doi.org/10.1007/978-94-009-9905-3, 1978.

Roberts, G. C., Day, D. A., Russell, L. M., Dunlea, E. J., Jimenez, J. L., Tomlinson, J. M., Collins, D. R., Shinozuka, Y., and Clarke, A. D.: Characterization of particle cloud droplet activity and composition in the free troposphere and the boundary layer during INTEX-B, Atmos. Chem. Phys., 10, 6627–6644, https://doi.org/10.5194/acp-10-6627-2010, 2010.

Rohanizadegan, M., Petrone, R. M., Pomeroy, J. W., Kosovic, B., Muñoz-Esparza, D., and Helgason, W. D.: High-Resolution Large-Eddy Simulations of Flow in the Complex Terrain of the Canadian Rockies, Earth Space Sci., 10, e2023EA003166, https://doi.org/10.1029/2023EA003166, 2023.

Rotach, M. W., Stiperski, I., Fuhrer, O., Goger, B., Gohm, A., Obleitner, F., Rau, G., Sfyri, E., and Vergeiner, J.: Investigating Exchange Processes over Complex Topography: The Innsbruck Box (i-Box), B. Am. Meteorol. Soc., 98, 787–805, https://doi.org/10.1175/BAMS-D-15-00246.1, 2017.

Sandu, I. and Stevens, B.: On the Factors Modulating the Stratocumulus to Cumulus Transitions, J. Atmos. Sci., 68, 1865–1881, https://doi.org/10.1175/2011JAS3614.1, 2011.

Sandu, I., Brenguier, J.-L., Geoffroy, O., Thouron, O., and Masson, V.: Aerosol impacts on the diurnal cycle of marine stratocumulus, J. Atmos. Sci., 65, 2705–2718, https://doi.org/10.1175/2008JAS2451.1, 2008.

Sato, Y., Nishizawa, S., Yashiro, H., Miyamoto, Y., Kajikawa, Y., and Tomita, H.: Impacts of cloud microphysics on trade wind cumulus: which cloud microphysics processes contribute to the diversity in a large eddy simulation?, Prog. Earth Planet. Sci., 2, 23, https://doi.org/10.1186/s40645-015-0053-6, 2015.

Schär, C., Fuhrer, O., Arteaga, A., Ban, N., Charpilloz, C., Di Girolamo, S., Hentgen, L., Hoefler, T., Lapillonne, X., Leutwyler, D., Osterried, K., Panosetti, D., Rüdisühli, S., Schlemmer, L., Schulthess, T. C., Sprenger, M., Ubbiali, S., and Wernli, H.: Kilometer-Scale Climate Models: Prospects and Challenges, B. Am. Meteorol. Soc., 101, E567–E587, https://doi.org/10.1175/BAMS-D-18-0167.1, 2020.

Schemann, V. and Ebell, K.: Simulation of mixed-phase clouds with the ICON large-eddy model in the complex Arctic environment around Ny-Ålesund, Atmos. Chem. Phys., 20, 475–485, https://doi.org/10.5194/acp-20-475-2020, 2020.

Schemann, V., Ebell, K., Pospichal, B., Neggers, R., Moseley, C., and Stevens, B.: Linking Large-Eddy Simulations to Local Cloud Observations, J. Adv. Model. Earth Syst., 12, e2020MS002209, https://doi.org/10.1029/2020MS002209, 2020.

Schmidli, J., Böing, S., and Fuhrer, O.: Accuracy of Simulated Diurnal Valley Winds in the Swiss Alps: Influence of Grid Resolution, Topography Filtering, and Land Surface Datasets, Atmosphere, 9, 196, https://doi.org/10.3390/atmos9050196, 2018.

Schmidt, H., Rast, S., Bao, J., Cassim, A., Fang, S.-W., Jimenez-de la Cuesta, D., Keil, P., Kluft, L., Kroll, C., Lang, T., Niemeier, U., Schneidereit, A., Williams, A. I. L., and Stevens, B.: Effects of Vertical Grid Spacing on the Climate Simulated in the ICON461.5-Sapphire Global Storm-Resolving Model, Geosci. Model Dev., 17, 1563–1584, https://doi.org/10.5194/gmd-17-1563-2024, 2024.

Schöni, F.: ICON Model Evaluation: A Cold Air Pool Case Study, MS thesis, ETH Zurich, https://doi.org/10.3929/ethz-b-000611435, 2023.

Schulz, J.-P. and Vogel, G.: Improving the Processes in the Land Surface Scheme TERRA: Bare Soil Evaporation and Skin Temperature, Atmosphere, 11, 513, https://doi.org/10.3390/atmos11050513, 2020.

Schulze, B. C., Charan, S. M., Kenseth, C. M., Kong, W., Bates, K. H., Williams, W., Metcalf, A. R., Jonsson, H. H., Woods, R., Sorooshian, A., Flagan, R. C., and Seinfeld, J. H.: Characterization of Aerosol Hygroscopicity Over the Northeast Pacific Ocean: Impacts on Prediction of CCN and Stratocumulus Cloud Droplet Number Concentrations, Earth Space Sci., 7, e2020EA001098, https://doi.org/10.1029/2020EA001098, 2020.

Seifert, A.: A Revised Cloud Microphysical Parameterization for COSMO-LME, COSMO Newsletter, 25–28, https://www.cosmo-model.org/content/model/documentation/newsLetters/newsLetter07/cnl7_seifert.pdf (last access: 3 April 2024), 2006.

Seifert, A. and Beheng, K. D.: A Two-Moment Cloud Microphysics Parameterization for Mixed-Phase Clouds. Part 1: Model Description, Meteorol. Atmos. Phys., 92, 45–66, https://doi.org/10.1007/s00703-005-0112-4, 2006.

Shima, S., Kusano, K., Kawano, A., Sugiyama, T., and Kawahara, S.: The super-droplet method for the numerical simulation of clouds and precipitation: a particle-based and probabilistic microphysics model coupled with a non-hydrostatic model, Q. J. Roy. Meteorol. Soc., 135, 1307–1320, https://doi.org/10.1002/qj.441, 2009.

Siebesma, A. P., Bretherton, C. S., Brown, A., Chlond, A., Cuxart, J., Duynkerke, P. G., Jiang, H. L., Khairoutdinov, M., Lewellen, D., Moeng, C. H., Sanchez, E., Stevens, B., and Stevens, D. E.: A large eddy simulation intercomparison study of shallow cumulus convection, J. Atmos. Sci., 60, 1201–1219, https://doi.org/10.1175/1520-0469(2003)60<1201:ALESIS>2.0.CO;2, 2003.

Simmel, M., Trautmann, T., and Tetzlaff, G.: Numerical solution of the stochastic collection equation – comparison of the Linear Discrete Method with other methods, Atmos. Res., 61, 135–148, https://doi.org/10.1016/S0169-8095(01)00131-4, 2002.

Singh, S., Kalthoff, N., and Gantner, L.: Sensitivity of convective precipitation to model grid spacing and land-surface resolution in ICON, Q. J. Roy. Meteorol. Soc., 147, 2709–2728, https://doi.org/10.1002/qj.4046, 2021.

Smagorinsky, J.: General circulation experiments with the primitive equations, Mon. Weather Rev., 91, 99–164, https://doi.org/10.1175/1520-0493(1963)091<0099:GCEWTP>2.3.CO;2, 1963.

Stevens, B., Aquistapache, C., Hansen, A., Heinze, R., Klinger, C., Klocke, D., Rybka, H., Schubotz, W., Windmiller, J., Adamidis, P., Arka, I., Barlakas, V., Biercamp, J., Brueck, M., Brune, S., Buehler, S. A., Burkhardt, U., Cioni, G., Costa-Surós, M., Crewell, S., Crüger, T., Deneke, H., Friedrichs, P., Henken, C. C., Hohenegger, C., Jacob, M., Jakub, F., Kalthoff, N., Köhler, M., van Laar, T. W., Li, P., Löhnert, U., Macke, A., Madenach, N., Mayer, B., Nam, C., Naumann, A. K., Peters, K., Poll, S., Quaas, J., Röber, N., Rochetin, N., Scheck, L., Schemann, V., Schnitt, S., Seifert, A., Senf, F., Shapkalijewski, M., Simmer, C., Singh, S., Sourdeval, O., Spickermann, D., Strandgren, J., Tessiot, O.,

Vercauteren, N., Vial, J., Voigt, A., and Zängl, G.: The Added Value of Large-eddy and Storm-resolving Models for Simulating Clouds and Precipitation, J. Meteorol. Soc. Jappn. Ser. II, 98, 395–435, https://doi.org/10.2151/jmsj.2020-021, 2020.

Stevens, B., Feingold, G., Cotton, W. R., and Walko, R. L.: Elements of the microphysical structure of numerically simulated nonprecipitating stratocumulus, J. Atmos. Sci., 53, 980–1006, https://doi.org/10.1175/1520-0469(1996)053<0980:EOTMSO>2.0.CO;2, 1996.

Stevens, D. E. and Bretherton, C. S.: Effects of resolution on the simulation of stratocumulus entrainment, Q. J. Roy. Meteorol. Soc., 125, 425–439, https://doi.org/10.1002/qj.49712555403, 1999.

Strauss, C., Ricard, D., Lac, C., and Verrelle, A.: Evaluation of Turbulence Parametrizations in Convective Clouds and Their Environment Based on a Large-Eddy Simulation, Q. J. Roy. Meteorol. Soc., 145, 3195–3217, https://doi.org/10.1002/qj.3614, 2019.

Tonttila, J., Maalick, Z., Raatikainen, T., Kokkola, H., Kuhn, T., and Romakkaniemi, S.: UCLALES-SALSA v1.0: a large-eddy model with interactive sectional microphysics for aerosol, clouds and precipitation, Geosci. Model Dev., 10, 169–188, https://doi.org/10.5194/gmd-10-169-2017, 2017.

Tukiainen, S., O'Connor, E., and Korpinen, A.: CloudnetPy: A Python Package for Processing Cloud Remote Sensing Data, J. Open Source Softw., 5, 2123, https://doi.org/10.21105/joss.02123, 2020.

Twohy, C. H., Anderson, J. R., Toohey, D. W., Andrejczuk, M., Adams, A., Lytle, M., George, R. C., Wood, R., Saide, P., Spak, S., Zuidema, P., and Leon, D.: Impacts of aerosol particles on the microphysical and radiative properties of stratocumulus clouds over the southeast Pacific Ocean, Atmos. Chem. Phys., 13, 2541–2562, https://doi.org/10.5194/acp-13-2541-2013, 2013.

Umek, L., Gohm, A., Haid, M., Ward, H. C., and Rotach, M. W.: Large eddy simulation of foehn-cold pool interactions in the Inn Valley during PIANO IOP2, Q. J. Roy. Meteor. Soc., 147, 944–982, https://doi.org/10.1002/qj.3954, 2021.

Van Weverberg, K., Goudenhoofdt, E., Blahak, U., Brisson, E., Demuzere, M., Marbaix, P., and van Ypersele, J.-P.: Comparison of one-moment and two-moment bulk microphysics for high-resolution climate simulations of intense precipitation, Atmos. Res., 147–148, 145–161, https://doi.org/10.1016/j.atmosres.2014.05.012, 2014.

Voordendag, A., Goger, B., Prinz, R., Sauter, T., Mölg, T., Saigger, M., and Kaser, G.: A novel framework to investigate wind-driven snow redistribution over an Alpine glacier: combination of high-resolution terrestrial laser scans and large-eddy simulations, The Cryosphere, 18, 849–868, https://doi.org/10.5194/tc-18-849-2024, 2024.

Walko, R., Cotton, W., Meyers, M., and Harrington, J.: New RAMS cloud microphysics parameterization part I: the single-moment scheme, Atmos. Res., 38, 29–62, https://doi.org/10.1016/0169-8095(94)00087-T, 1995.

Wang, Z.-C., Yin, B., Min, Q., and Zhu, L.: Temperature-dependence of the near-UV absorption of water vapor in the 290–350 nm range, J. Quant. Spectrosc. Ra., 28, 108204, https://doi.org/10.1016/j.jqsrt.2022.108204, 2022.

Wegener, A.: Thermodynamik der Atmosphäre, Barth, 1911.

Witte, M. K., Morrison, H., Davis, A. B., and Teixeira, J.: Limitations of Bin and Bulk Microphysics in Reproducing the Observed Spatial Structure of Light Precipitation, J. Atmos. Sci., 79, 161–178, https://doi.org/10.1175/JAS-D-21-0134.1, 2022.

Xue, H., Feingold, G., and Stevens, B.: Aerosol effects on clouds, precipitation, and the organization of shallow cumulus convection, J. Atmos. Sci., 65, 392–406, https://doi.org/10.1175/2007JAS2428.1, 2008.

Yamaguchi, T. and Feingold, G.: Technical note: Large-eddy simulation of cloudy boundary layer with the Advanced Research WRF model, J. Adv. Model. Earth Syst., 4, M09003, https://doi.org/10.1029/2012MS000164, 2012.

Zängl, G., Reinert, D., Rípodas, P., and Baldauf, M.: The ICON (ICOsahedral Non-hydrostatic) Modelling Framework of DWD and MPI-M: Description of the Non-Hydrostatic Dynamical Core, Q. J. Roy. Meteorol. Soc., 141, 563–579, https://doi.org/10.1002/qj.2378, 2015.

Zhang, Y., Klein, S. A., Fan, J., Chandra, A. S., Kollias, P., Xie, S., and Tang, S.: Large-Eddy Simulation of Shallow Cumulus over Land: A Composite Case Based on ARM Long-Term Observations at Its Southern Great Plains Site, J. Atmos. Sci., 74, 3229–3251, https://doi.org/10.1175/JAS-D-16-0317.1, 2017.